Journal of Building Engineering 118 (2026) 114971



Contents lists available at ScienceDirect

Journal of Building Engineering

journal homepage: www.elsevier.com/locate/jobe



Time-dependent numerical modelling of conventional and geopolymer concrete beams serviceability

Yuan Dong [a,*], Jun Li [a], Shami Nejadi [a], Tengfei Xu [b], Arnaud Castel [a]

[a] School of Civil and Environmental Engineering, University of Technology Sydney, Australia
[b] Department of Bridge Engineering, School of Civil Engineering, Southwest Jiaotong University, Chengdu, 610031, PR China

ARTICLE INFO

Keywords:
Creep
Shrinkage
Damage
Serviceability
Finite element analysis.
Geopolymer concrete

ABSTRACT

Controlling deflection in reinforced concrete structures is essential for ensuring serviceability and long-term performance. This study presents a numerical approach to simulate the effects of short-term and long-term service loading on reinforced concrete flexural members, validated against data from experimental investigations conducted at the UNSW Australia including conventional concrete and heat-cured low calcium fly ash geopolymer concrete. The creep coefficient and shrinkage of concrete were calibrated using MATLAB's nonlinear fitting function. AS3600-2018 standard creep and shrinkage models were used for conventional concrete beams. Experimental creep and shrinkage data were used for the geopolymer concrete beam. A three-dimensional finite element analysis (FEA) model was developed in ABAQUS, incorporating creep and shrinkage effects through user subroutines (USDFLD, UEXPAN, and GETVRM) within the concrete damage plasticity (CDP) framework. The model was employed to analyze the short-term deflection after cracking, time-dependent deflection under sustained loading, and long-term stiffness degradation of reinforced concrete beams. The numerical results were successful compared to the experimental results obtained on conventional and geopolymer concrete beams, demonstrating the accuracy and effectiveness of the proposed approach.

1. Introduction

Creep and shrinkage can result in various forms of damage in concrete structures, whether prestressed, reinforced, or unreinforced. Over time, creep may cause excessive deflection and cracking in bridges and buildings, significantly reducing service life. Controlling deflection in reinforced concrete structures is essential to ensure both serviceability and long-term durability [1,2]. Excessive deformation is one of the primary causes of deterioration and results in substantial maintenance costs in the construction industry. Among the long-term effects, shrinkage and creep significantly influence concrete structures time-dependent deformation and stiffness degradation [3,4]. If not adequately considered during the design phase, these effects can lead to excessive cracking, loss of load-bearing capacity, and severe serviceability issues [5].

Many numerical methods have been proposed to simulate concrete creep and shrinkage, including step-by-step integration and single-step algebraic formulations [6]. Single-step methods, such as the effective modulus (EM) method, mean stress (MS) method, and age-adjusted effective modulus (AAEM) method, simplify the numerical implementation, but they are no longer sufficient to meet practical engineering demands [6–9]. These methods often overlook critical factors such as material nonlinearity, progressive damage

* Corresponding author.
E-mail address: Yuan.Dong@student.uts.edu.au (Y. Dong).

https://doi.org/10.1016/j.jobe.2025.114971
Received 11 August 2025; Received in revised form 5 December 2025; Accepted 12 December 2025
Available online 14 December 2025
2352-7102/© 2025 The Authors. Published by Elsevier Ltd. This is an open access article under the CC BY license (http://creativecommons.org/licenses/by/4.0/).

accumulation, and stress redistribution due to microcrack formation. Furthermore, all these methods fail to capture the damage evolution behaviour of concrete structures, which is essential for accurately predicting long-term performance.

While some studies have developed models capable of capturing the instantaneous stiffness degradation of concrete structures [10], they fail to accurately represent the creep induced long-term stiffness reduction. Conversely, existing models that focus on long-term stiffness degradation primarily address gradual creep effects on deflection increase under sustained loading while neglecting short-term stiffness loss assessed through loading cycles post-concrete cracking [11]. Although such approaches are suitable for ultra-high-performance concrete (UHPC) beams, they are less applicable to conventional concrete structures, where early-stage microcrack formation and stress redistribution significantly influence the structural performance. Short-term stiffness degradation can have a pronounced impact on transient structural response, necessitating a modelling approach that accounts for both immediate and progressive stiffness evolution. Meanwhile, it should be noted that most of these recent studies have modelled concrete beams using beam or shell elements, which, although computationally efficient, cannot accurately capture the localized cracking, stress redistribution, and damage progression in the concrete body. In contrast, this study employs C3D8 solid elements, which offer substantially higher spatial resolution and can reproduce both instantaneous and time-dependent stiffness degradation in concrete. Furthermore, some studies ignored the concrete shrinkage in the simulations. Therefore, relying solely on long-term creep models may lead to an incomplete characterization of deformation and damage evolution across different timescales [9–13].

Despite its distinct chemical composition and reaction mechanisms, geopolymer concrete exhibits many characteristics of conventional Portland cement-based concrete [13–16]. It offers similar mechanical strength, and workability while providing advantages such as lower carbon emissions, enhanced chemical resistance, and reduced creep deformation [17]. In a previous study [18], authors reported that both compressive creep and shrinkage of heat cured low calcium fly ash geopolymer concrete can be very low compared to traditional Portland cement-based concrete. These properties make geopolymer concrete a promising alternative to traditional Portland cement-based concrete, particularly in applications requiring improved sustainability and long-term performance. However, variations in microstructural development, hydration mechanisms, and long-term behaviour necessitate further investigation to fully understand geopolymer concrete response under sustained loading conditions [18–20].

Meanwhile, the database for geopolymer concrete (GPC) is newer and more heterogeneous. Reported trends depend on precursor chemistry (low-calcium fly ash vs. slag-blended binders), activator concentration, and curing regime (heat-cured vs. ambient-cured). Several studies observed comparable or reduced basic creep but pronounced drying shrinkage sensitivity relative to OPC, while others reported mix-specific divergences, indicating that OPC-calibrated models may not transfer directly to GPC without re-parameterization. This variability underscores the need for member-level validations where shrinkage and creep jointly drive serviceability [13,15].

The long-term behaviour of geopolymer concrete remains a subject of ongoing research, particularly regarding its time-dependent stiffness evolution and resistance to cracking under sustained loads. Unlike Portland cement-based concrete, which undergoes significant hydration-driven shrinkage and creep, geopolymer concrete develops strength through polymerization reactions, which could lead to different time-dependent mechanical responses. The role of precursor materials, activator types, and curing conditions further complicates the prediction of geopolymer concrete long-term performance. Additionally, while laboratory studies have demonstrated reduced creep deformation, real-world applications require further validation through field monitoring and full-scale structural assessments. Addressing these knowledge gaps is crucial for optimizing geopolymer concrete formulations and ensuring their reliability in structural applications over extended service periods [20,21].

This study focuses on several key aspects of long-term serviceability: (1) finite element analysis (FEA) of the time-dependent increase in reinforced concrete beams deflection under sustained loading, (2) finite element analysis (FEA) of the stiffness degradation of reinforced concrete beams subjected to loading cycles following an extended period under sustained loading, and (3) comparison between the performance of conventional Portland cement-based concrete beams and heat cured low calcium fly ash geopolymer concrete beams. These aspects are critical for understanding the mechanical response of concrete structures and improving predictive modelling techniques for serviceability design of both conventional and low carbon concrete structures.

To address the limitations of existing concrete creep analysis methods in ABAQUS, this research developed a user subroutine for creep and shrinkage modelling, integrating a step-by-step numerical approach within the Concrete Damage Plasticity (CDP) framework. Experimental results from the literature are used to validate the 3-Dimensional creep analysis model in ABAQUS implemented through the user subroutine proposed. Experiments were carried out at the University of New South Wales (UNSW) Australia for both conventional Portland cement-based concrete beams [10] and heat cured low calcium fly ash geopolymer concrete beams [21]. For geopolymer concrete, all concrete mechanical properties were measured experimentally including long-term compressive creep coefficient and total shrinkage. For Portland cement-based concrete, Australian Standards AS3600 creep and shrinkage models were used as these concrete properties were not experimentally assessed. Using the developed ABAQUS subroutine and the experimental data, finite element (FE) models for conventional and heat cured low calcium fly ash geopolymer concrete beams were constructed to investigate the impact of creep and shrinkage on both time-dependent stiffness degradation and long-term beams deflection focusing on serviceability.

2. Numerical modelling and creep analysis method

Numerical formulations for compressive creep in FEA software can be broadly classified into differential-type constitutive relations and incremental constitutive relations. Both approaches eliminate the need to store the full stress history, enhancing computational efficiency. The incremental constitutive relation was adopted in this study due to its ability to efficiently capture the time-dependent stress redistribution while maintaining numerical stability, especially in long-term simulations.

The total strain in concrete at any given time consists of the following components:

$$\varepsilon(t) = \varepsilon_e(t) + \varepsilon_p(t) + \varepsilon_c(t) + \varepsilon_s(t) \tag{1}$$

In the above equation $\varepsilon_e(t)$ is the elastic strain, $\varepsilon_p(t)$ is the plastic strain, $\varepsilon_c(t)$ is the creep strain, $\varepsilon_s(t)$ is the shrinkage strain. Creep coefficient, specific creep, and creep compliance are the three essential functions that can be expressed as shown by equations (2)–(4) respectively [22].

The creep coefficient can be expressed as:

$$\phi(t,\tau) = E_c * \frac{\varepsilon_c(t)}{\sigma(\tau)} = \frac{\varepsilon_c(t)}{\varepsilon_e(\tau)} \tag{2}$$

The specific creep can be expressed as:

$$C(t,\tau) = \frac{\phi(t,\tau)}{E_c} = \frac{\varepsilon_c(t)}{\sigma(\tau)} \tag{3}$$

The creep compliance refers to the creep strain produced in concrete at time t under a unit constant stress applied since time τ, which is the first loading day of the concrete. The creep compliance can be expressed as:

$$J(t,\tau) = \frac{1+\phi(t,\tau)}{E_c} = \frac{\varepsilon_c(t)}{\sigma(\tau)} + \frac{1}{E_c} = \frac{\varepsilon_c(t)}{\sigma(\tau)} + \frac{\varepsilon_c(\tau)}{\sigma(\tau)} \tag{4}$$

Based on the above functions a numerical model for creep analysis is developed in the next section, including concrete shrinkage.

2.1. Three-dimensional creep effect of concrete

In order to accurately capture the lateral deformation effects induced by creep, a Poisson's ratio matrix [A] is used to describe the relationship between stress and strain in different directions, and the derivation can be seen below equation (5) [22].

$$[A] = \begin{bmatrix} 1 & -\upsilon & -\upsilon & 0 & 0 & 0 \\ -\upsilon & 1 & -\upsilon & 0 & 0 & 0 \\ -\upsilon & -\upsilon & 1 & 0 & 0 & 0 \\ 0 & 0 & 0 & 2(1+\upsilon) & 0 & 0 \\ 0 & 0 & 0 & 0 & 2(1+\upsilon) & 0 \\ 0 & 0 & 0 & 0 & 0 & 2(1+\upsilon) \end{bmatrix} \tag{5}$$

The above equation can be derived from generalized Hooke's law, assuming that concrete is an isotropic material. The stiffness matrix can be expressed as follows:

$$[D] = \begin{bmatrix} \frac{1}{E} & -\frac{-\upsilon}{E} & \frac{-\upsilon}{E} & 0 & 0 & 0 \\ -\frac{-\upsilon}{E} & \frac{1}{E} & -\frac{-\upsilon}{E} & 0 & 0 & 0 \\ -\frac{-\upsilon}{E} & -\frac{-\upsilon}{E} & \frac{1}{E} & 0 & 0 & 0 \\ 0 & 0 & 0 & \frac{1}{G} & 0 & 0 \\ 0 & 0 & 0 & 0 & \frac{1}{G} & 0 \\ 0 & 0 & 0 & 0 & 0 & \frac{1}{G} \end{bmatrix} \tag{6}$$

$$\begin{bmatrix} \varepsilon_{xx} \\ \varepsilon_{yy} \\ \varepsilon_{zz} \\ 2\varepsilon_{yz} \\ 2\varepsilon_{zx} \\ 2\varepsilon_{xy} \end{bmatrix} = \begin{bmatrix} \frac{1}{E} & -\frac{-\upsilon}{E} & \frac{-\upsilon}{E} & 0 & 0 & 0 \\ -\frac{-\upsilon}{E} & \frac{1}{E} & -\frac{-\upsilon}{E} & 0 & 0 & 0 \\ -\frac{-\upsilon}{E} & -\frac{-\upsilon}{E} & \frac{1}{E} & 0 & 0 & 0 \\ 0 & 0 & 0 & \frac{1}{G} & 0 & 0 \\ 0 & 0 & 0 & 0 & \frac{1}{G} & 0 \\ 0 & 0 & 0 & 0 & 0 & \frac{1}{G} \end{bmatrix} \begin{bmatrix} \sigma_{xx} \\ \sigma_{yy} \\ \sigma_{zz} \\ \sigma_{yz} \\ \sigma_{zx} \\ \sigma_{xy} \end{bmatrix} \tag{7}$$

By substituting the shear module, the Poisson's ratio matrix [*A*] is deduced:

$$G = \frac{E}{2^*(1+\upsilon)} \tag{8}$$

2.2. Stepwise creep incremental analysis method

For a concrete structure subjected to a first loading time of τ, the total strain at time t is composed of three parts. The first part is the elastic strain and plastic strain at time t. The second part accounts for the creep strain generated by the load increments over the interval $(t-\tau)$. The third part includes the shrinkage strain ε_s. By introducing the influence of creep Poisson's ratio, the three-dimensional nonlinear creep strain constitutive relationship can be expressed as follows:

$$\{\varepsilon(t)\} = [A]\{\sigma(t)\} \int_{\tau}^{t} J(t,\tau,\sigma)[A]\left\{\frac{d\sigma(t)}{d\tau}\right\} d\tau + \{\varepsilon_s\} \tag{9}$$

$$J(t,\tau,\sigma) = \frac{1+\phi(t,\tau)}{E_c(1-d(\tau))} = C(t,\tau,\sigma) + \frac{1}{E_c(1-d(\tau))} \tag{10}$$

Where σ is the stress Component Matrix, which is equal to $\left[\sigma_x, \sigma_y, \sigma_z, \sigma_{xy}, \sigma_{xz}, \sigma_{yz}\right]^T$

ε is the strain Component Matrix, which is equal to $\left[\varepsilon_x, \varepsilon_y, \varepsilon_z, \varepsilon_{xy}, \varepsilon_{xz}, \varepsilon_{yz}\right]^T$

In the above equation $J(t,\tau,\sigma)$ is the creep compliance at the time (t) relative to the concrete first loading time τ. The function C (t, τ) (Equation (11)) represents the specific creep compliance at time t during a loading period, τ means the first loading time of a concrete structure. Using Dirichlet series to represent this equation, as shown in equations (12) and (13), this approach allows for flexibility in fitting various creep prediction models and avoids the need for stress history integration across the entire period.

$$\mathrm{C}(\mathrm{t},\tau) = \sum_{1}^{\mathrm{m}} \mathrm{a_i}\left[1 - \mathrm{e}^{-\lambda(\mathrm{t}-\tau)}\right] \tag{11}$$

$\mathrm{E_c(t)}$: Represents the elastic modulus of concrete at time t during the loading period.

d(τ): Damage factor at time τ, related to the stress state of concrete, with values in the range [0,1].

The undetermined parameters α_i are determined by the following steps (from equation (12)–(17)):

$$C(t,\tau,\sigma) = \frac{1}{(1-d(\tau))} \sum_{1}^{m} a_i\left[1 - e^{-\lambda(t-\tau)}\right] \tag{12}$$

$$C(t,\tau) = \sum_{1}^{m} a_i\left[1 - e^{-\lambda(t-\tau)}\right] \tag{13}$$

Appropriate values for m and λi are selected to achieve desired accuracy, which are discrete retardation constants introduced in the series expansion to capture the time-dependent creep behaviour of concrete. with typical values $m = 5$, $\lambda_1 = 1$, $\lambda_2 = 0.1$, $\lambda_3 = 0.01$, $\lambda_4 = 0.001$, $\lambda_5 = 0.0001$ [6]. Then, the creep time (t) and the first loading time (τ) for concrete are defined. If the creep strain is calculated incrementally, (t-τ) is divided into some intervals. For each interval, either a creep prediction model or creep experiment data can be used to calculate the creep coefficient and introduced into the following equations:

$$[N]_{n^*m}{}^*[a]_{m^*1} = [b]_{n^*1} \tag{14}$$

$$[N]_{n^*m} = \begin{bmatrix} 1-e^{-\lambda_1(t_1-\tau)} & \cdots & 1-e^{-\lambda_5(t_1-\tau)} \\ \vdots & \ddots & \vdots \\ 1-e^{-\lambda_1(t_n-\tau)} & \cdots & 1-e^{-\lambda_m(t_n-\tau)} \end{bmatrix} \tag{15}$$

By using the least-squares method, the coefficient a i can be determined as follows:

$$[a]_{m^*1} = \left[N^T N\right]^{-1}_{m^*m} * \left[N^T b\right]_{m^*1} \tag{16}$$

In the above equation, the matrix b can be expressed as follows.

$$[a]_{m^*1} = [a_1(\tau), a_2(\tau) \cdots a_m(\tau)]^T, [b]_{n^*1} = [C(t_1,\tau), C(t_2,\tau) \cdots C(t_n,\tau)]^T \tag{17}$$

The creep coefficient and shrinkage strain functions were calibrated using MATLAB's nonlinear least-squares fitting procedure. The experimental data for shrinkage, creep coefficient were imported from laboratory measurements or concrete shrinkage or creep prediction model, and the time-dependent responses were fitted using a multi-exponential function showed in equation (13). Fig. 1 shows an example of the Dirichlet series fitted to AS3600 creep coefficient and shrinkage strain models.

2.3. Incremental creep strain calculation

Concrete shrinkage is independent of the stress history and can be directly incorporated into the finite element (FE) model. In contrast, creep behaviour is stress-dependent and requires an appropriate numerical implementation. The creep coefficient of Portland cement-based concrete used in this study was calculated based on AS3600-2018 model, which provides empirical equations for predicting the time-dependent creep strain under sustained loading.

Concrete compressive creep has a significant impact on the long-term structural behaviour of concrete structures. If structural system transitions occur during construction, shrinkage-induced secondary internal forces may also cause corresponding creep deformations. Additionally, the secondary internal forces resulting from creep deformations will further influence subsequent creep deformations. Among various analysis methods, the stepwise recursive analysis approach is particularly practical for handling this complex process. It is also compatible with general finite element software, making it widely used in practical engineering. The three-dimensional mechanical model for shrinkage and creep effects used in this research is based on Li method [6].

The creep strain at time t_n and time t_{n-1} can be expressed as following:

$$\{\varepsilon(t_n)\} = [A][\{\Delta\sigma_0\}C(t_n,t_0,\sigma_{t0}) - C(t_n,t_0,\sigma_{t0})] + \cdots + [\{\Delta\sigma_{n-1}\}C(t_n,t_{n-1},\sigma_{t0}) - C(t_n,t_{n-1},\sigma_{tn-1})] \tag{18}$$

$$\{\varepsilon(t_{n-1})\} = [A][\{\Delta\sigma_0\}C(t_{n-1},t_0,\sigma_{t0}) - C(t_{n-1},t_0,\sigma_{t0})] + \cdots + [\{\Delta\sigma_{n-2}\}C(t_n,t_{n-2},\sigma_{t0}) - C(t_{n-1},t_{n-2},\sigma_{tn-2})] \tag{19}$$

Thus, the creep increment can be calculated as:

$$\{\Delta\varepsilon(t_n)\} = \{\varepsilon(t_n)\} - \{\varepsilon(t_{n-1})\} \tag{20}$$

Meanwhile, based on equations (21) and (22), the creep strain increment can be calculated by using Equation (23).

$$C(t_n,t_j,\sigma_{tj}) - C(t_{n-1},t_j,\sigma_{tj}) = \frac{1}{(1-d(\tau))}\left(\sum_{j=1}^{m} a_j(t_j)\left[1-e^{-\lambda_j(t_n-t_j)}\right] - \sum_{j=1}^{m} a_j(t_j)\left[1-e^{-\lambda_j(t_{n-1}-t_j)}\right]\right) \tag{21}$$

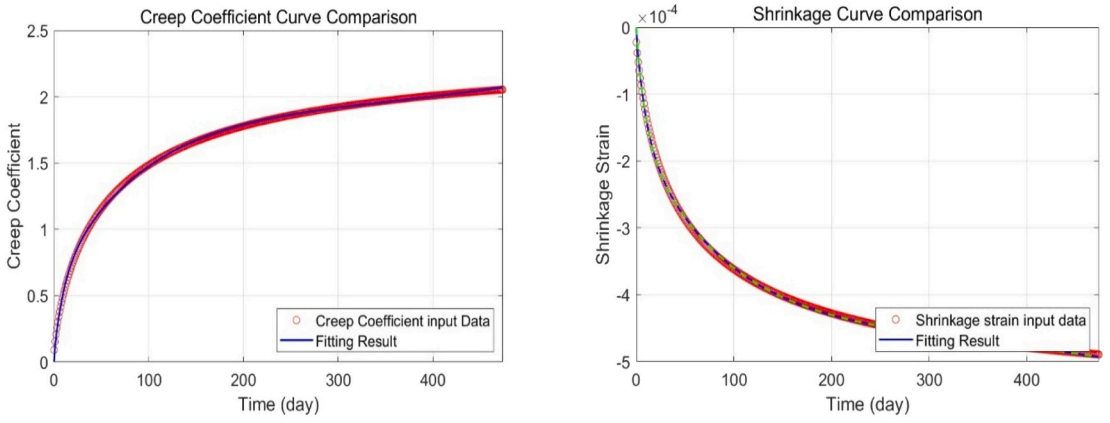


Fig. 1. Creep coefficient and shrinkage fitting curve using MATLAB.

$$C(t_n, t_j, \sigma_{ij}) - C(t_{n-1}, t_j, \sigma_{ij}) = \frac{1}{(1 - d(\tau))} \sum_{j=1}^{m} a_i t_j \left[e^{-\lambda_i (t_{n-1} - t_j)}\right] \left[1 - e^{-\lambda_i \Delta t_n}\right] \tag{22}$$

$$\{\Delta\varepsilon(t_n)\} = \sum_{i=1}^{m} \left\{\omega(i, n-1)\left(1 - e^{-\lambda_i \Delta t_n}\right)\right\} \tag{23}$$

In the above equation,

$$\omega(i, 1) = \frac{1}{(1 - d(\tau))} [A]\{\Delta\bar{\sigma}_0\} a_i(t_0) \tag{24}$$

$$\omega(i, n) = \frac{1}{(1 - d(t_{n-1}))} \left\{\omega(i, n-1)\left(e^{-\lambda_i \Delta t_{n-1}}\right)\right\} + \frac{1}{(1 - d(t))} [A]\{\Delta\bar{\sigma}_n\} a_i(t_n) \tag{25}$$

In the above equation $d(\tau)$ is the damage factor of the concrete which is calculated by the concrete damage plasticity model. The above equation is derived from the recursive approach used in the stepwise creep analysis, where creep strain increments are calculated based on discrete time steps. This method allows to account for the complex time-dependent effects of concrete under sustained load without requiring performing continuous integrations over the entire loading period. By calculating the incremental changes in creep strain at each step, the cumulative effects of creep in structural analysis can be effectively modelled [6].

The conception of the stepwise method to calculate the concrete creep behaviour is represented in Fig. 2.

2.4. Algorithm for calculating concrete creep and shrinkage effect

In ABAQUS, two user subroutines (USDFLD and UEXPAN) along with a function (GETVRM) are utilized to analyze concrete creep effects. The USDFLD subroutine is used to define the evolving elastic modulus as a function of damage. At each time step, USDFLD assigns this varying elastic modulus. The UEXPAN subroutine calculates the incremental creep strain during each step based on shrinkage and creep effects. However, since the creep increment depends on stress levels, it requires values from previous time steps to perform the calculations. Therefore, state-dependent variables (SDVs) are used to store values from each time step and are accessible in the UEXPAN subroutine to compute the incremental strain. The state-dependent variables (SDVs) are employed to store the internal variables of the material at each integration point, enabling the subroutines to exchange historical information between successive time increments. These variables record both the instantaneous stress state and the accumulated time-dependent effects of creep and shrinkage.

Specifically, the SDVs contain the current and previous step stress components in six directions (normal and shear), the corresponding stress increments, and the accumulated values used for evaluating the creep compliance function. In addition, the previous step time and time increment are stored in the UEXPAN subroutine. The total shrinkage strain and the creep strain components are updated and saved at each increment in SDVs, allowing the subroutines to reconstruct the full-time history of deformation.

This approach allows ABAQUS to simulate concrete time-dependent creep and shrinkage. The overall interaction between the subroutines and the finite element solver, and how the subroutine works in ABAQUS is schematically illustrated in Fig. 3.

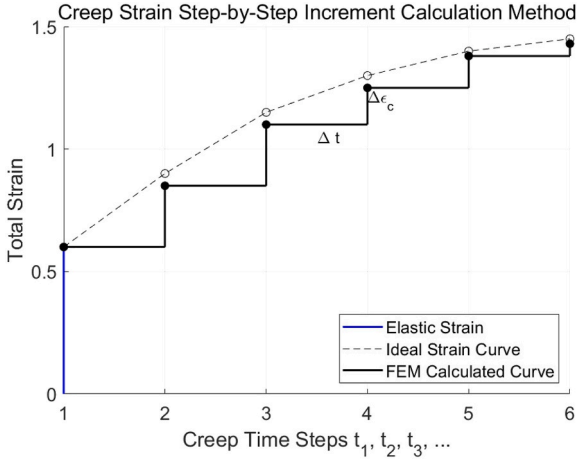


Fig. 2. Creep analysis method used in ABAQUS subroutine.

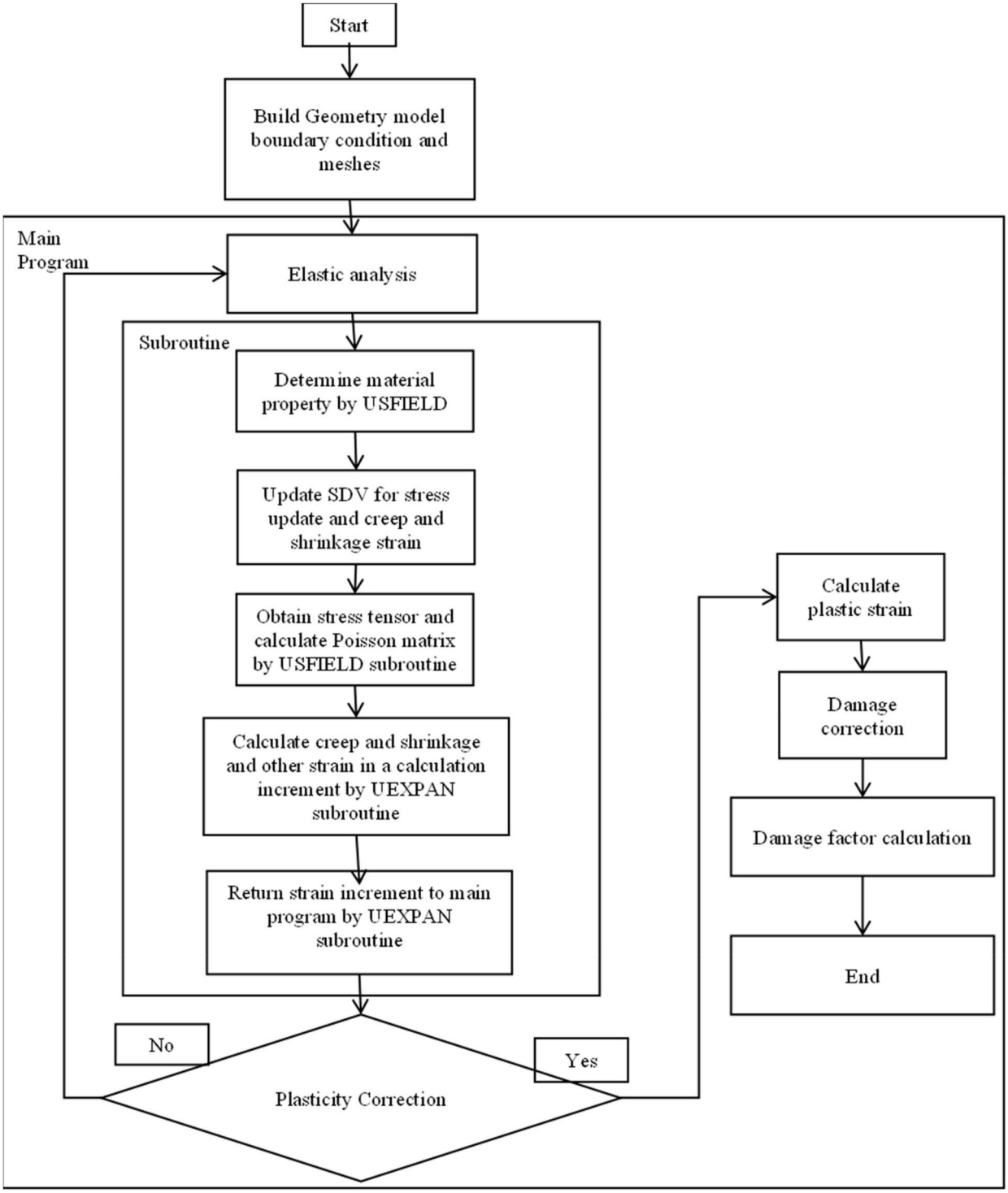


Fig. 3. Flowchart of subroutine calculation procedure.

2.5. Properties of material

2.5.1. Reinforcing bars

The steel elasto-plastic model in tension used in the simulations is presented in Fig. 4 In this study, the serviceability of the reinforced concrete beams was evaluated under a range of load levels not exceeding 50 % of the ultimate capacity of the beams.

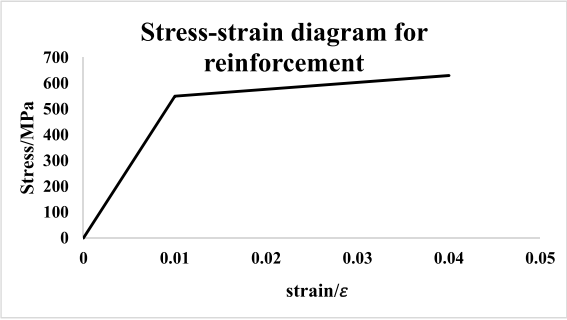


Fig. 4. Reinforcement behaviour in tension used in the simulations.

Reinforcement did not yield in any of the cases considered. Accordingly, steel reinforcement is assumed to remain within a purely elastic range, characterized by a Young's modulus of 200 GPa, for all cases considered in this study.

2.5.2. Nonlinear concrete material setting

In this research, the CDP model is based on the equivalent stress theory which expressed in equations 26 and 27. The effective stress is governed by the elastoplastic theory [23].

$$\sigma = (1 - D)\overline{\sigma} \tag{26}$$

D is the damage factor the element.

$\overline{\sigma}$ is the effective stress

$$\overline{\sigma} = E(\varepsilon - \varepsilon_p) \tag{27}$$

ε_p is the plastic strain of the concrete elements

E if the initial undamaged concrete elastic modulus.

The fundamental plastic parameters of the CDP model are shown in Table 1 [23,24]. Values presented in Table 1 were calibrated for Portland cement based concrete. But, the same values are also used for geopolymer concrete. Indeed, this numerical investigation is focusing on serviceability. As a result, the concrete in compression will remain mostly within its linear elastic phase and damage related parameters will only have a marginal impact on the simulations.

•The dilation angle $\psi = 38^{\circ}$, which is used in the non-associated flow potential function of the CDP model.

- The eccentricity $\varepsilon = 0.1$, defining the flow potential characteristics.
- The biaxial-to-uniaxial compression ratio fb0/fc0 = 1.16, and yield shape parameter k = 0.666667.
- The viscosity parameter $\mu = 0.001$ to aid convergence without significantly affecting physical accuracy.

The damage factor is calculated using Equation (28).

$$D = \begin{cases} \left[1 - \left(1 - \dfrac{\varepsilon}{\varepsilon_p}\right)^{c1}\right] D_0 & \varepsilon \le \varepsilon_p \\ 1 - \dfrac{1 - D_0}{C_2(1 - D_0)\left(\frac{\varepsilon}{\varepsilon_p} - 1\right)^{c3} + 1} & \varepsilon > \varepsilon_p \end{cases} \tag{28}$$

D_0 represents the damage value of concrete at peak stress. For uniaxial compression, the strain ε_p denotes the peak compressive strain, with $\varepsilon_c = 383\, f_{cu}^{7/18} * 10^{-6}$. For uniaxial tension, given by $\varepsilon_c = 33\, fc_{cu}^{1/3} * 10^{-6}$. The expressions for D_0, c_1 c_2 and c_3 are obtained from Table 2. The material parameters used in this study are consistent with typical values for brittle materials such as geopolymer and conventional concrete. For the same reason as for the concrete plastic properties presented in Table 1, the same damage properties are used for conventional concrete and geopolymer concrete.

The tensile and compressive stress-strain behaviour of concrete under the damage plasticity model are illustrated in Fig. 5 The short-term and long-term stiffness of both the GPC and OPC specimen were determined in ABAQUS through the Concrete Damaged

Table 1
Conventional and geopolymer concrete plastic properties.

Dilation	Eccentricity	fb0/fc0	k	Viscosity
38	0.1	1.16	0.666667	0.001

Table 2
Conventional and geopolymer concrete damage Properties.

Uniaxial Compression	Uniaxial Tension
$D_0 = 2.1 - 0.4 \ln (fc_{cu} + 41)$	$D_0 = 0.19$
$c_1 = 0.56 - 0.004 f_{cu}$	$c_1 = 0.31$
$c_2 = 1.17 + 4.34{*}10^{-5} f_{cu}^{2.8}$	$c_2 = 1.56 + 1.83{*}10^{-4} f_{cu}^{2.08}$
$c_2 = 0.32 + 0.3 \ln (f_{cu} - 10)$	$c_3 = 1.1 + 3.54{*}10^{-3} f_{cu}$

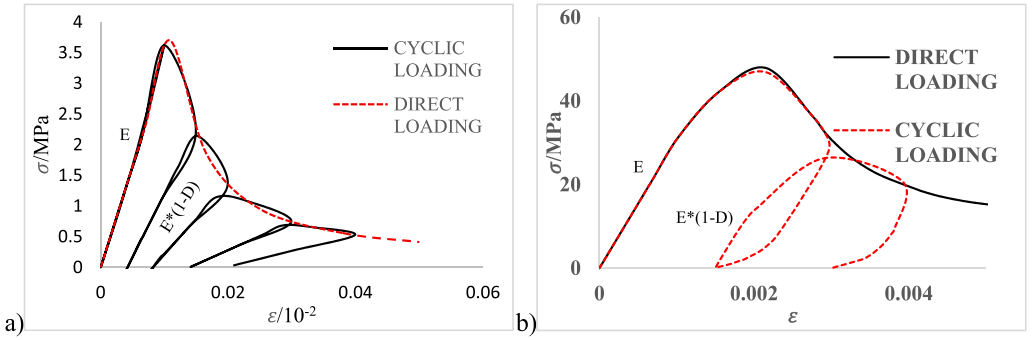


Fig. 5. Concrete behaviour (a) in tension and (b) in compression used in the simulations.

Plasticity (CDP) model. The CDP formulation intrinsically accounts for stiffness degradation under cyclic and sustained loading by updating the elastic modulus according to the evolving damage and inelastic strain. However, this numerical investigation is focusing on serviceability, the concrete in compression will remain mostly within its linear elastic phase, concrete compressive softening is not the primary focus of this paper. Only the tensile stress-strain behaviour of concrete under the damage plasticity model (Fig. 5a) will be governing the serviceability of the reinforced concrete beams post-concrete cracking.

3. Experimental program

3.1. Overview of the experimental program

To validate the accuracy of the developed finite element model, two experimental studies were selected.

- Case 1: Conventional Concrete Beams [10].
- Case 2: Low Calcium Fly Ash Geopolymer Concrete Beams [21].

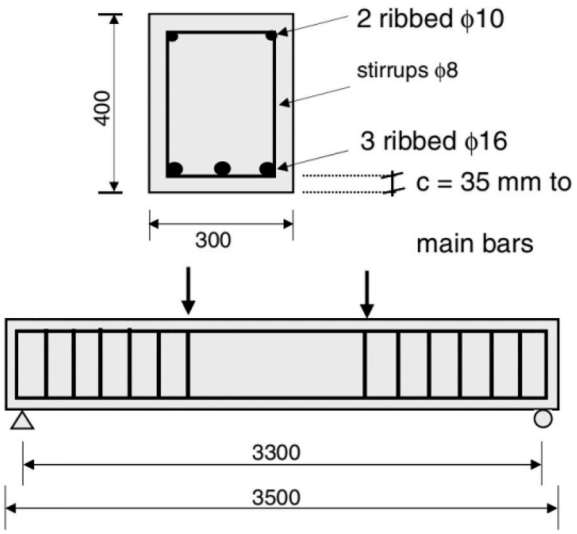


Fig. 6. Design of the conventional reinforced concrete beams.

These experiments aimed to evaluate the instantaneous stiffness of reinforced concrete beams after cracking through loading cycles under a loading and unloading rate of 0.1 mm/min, the long-term deflection increase under sustained loading and the reduction in instantaneous stiffness following the period of sustained loading, assessed by applying the same loading cycles as for the pre-cracking phase. The mechanical properties of concrete, experimental setup, and test results from both cases were used to validate the finite element simulations performed in ABAQUS.

3.2. Case 1: conventional concrete

The paper [10] presents findings from tests conducted on five reinforced concrete beams using Portland cement-based concrete. The mechanical properties of the concrete, measured under standard conditions (temperature $T = 20^{0}$C and relative humidity RH = 100 %), are as follows: mean compressive strength $f_{cm} = 46$ MPa, elastic modulus, $E_c = 33$ GPa, flexural tensile strength, $f`_{ct,f} = 3.5$ MPa. The compressive strength and elastic modulus were obtained from tests on standard (AS 1012.9 and AS 1012.17) cylindrical specimens, whereas the flexural tensile strength was determined from flexural tests by AS 1012.11. Each beam is 3500 mm in length with a 3000 mm span between supports and a cross-sectional dimension of 400 mm × 300 mm. The reinforcement layout is illustrated in Fig. 6. The main longitudinal steel bars used in each specimen are standard Australian deformed bars with a diameter of 16 mm (designated as N16). A concrete cover of 35 mm is provided for all beams. To avoid the influence of stirrups on crack locations and spacing, no stirrups were placed in the constant bending moment zone. The characteristic yield stress of the steel bars (elastic limit) is $f_y = 500$ MPa.

All beams were cast using the same batch of ready-mix concrete. The concrete was compacted using a vibrating needle. 24 h after casting and until the load tests commenced at age 28 days, some of the beams (labeled B2 and B3) were stored in a high moisture environment to reduce the drying shrinkage to as close to zero as possible. However, other beams were moist cured for only seven days and then stored in the laboratory (labeled B5 and B6 with pre-loading concrete shrinkage). For these beams, drying commenced at age seven days and significant shrinkage developed prior to first loading.

The sequences of the loading tests include a first monotonic loading at 28 days up to the peak loading values defined in Table 3 for each beam. The maximum load applied ranged from 33 % to 50 % of the Steel Yield Load (SYL) measured at 180 kN [10]. Then, loading cycles are applied to assess the beam stiffness after cracking without exceeding the peak loading value, defined as short-term stiffness. The beams are then subjected to a sustained load (load values provided in Table 3, ranging from 22 % to 50 % of the SYL) for about 250 days. Following the sustained loading period, the reinforced concrete beams are subjected to the same loading cycles to assess the stiffness reduction due to long term effects, define as long-term stiffness.

3.3. Case 2 geopolymer concrete

Similar experiments to case 1 relating to serviceability were conducted using heat-cured low calcium fly ash geopolymer concrete beams. The hardened properties of the heat-cured geopolymer concrete, including compressive strength, tensile strength, and instantaneous elastic modulus, were evaluated at 28 days using cylindrical specimens with dimensions of 100 mm in diameter and 200 mm in height. The uniaxial compressive strength was determined in accordance with ASTM C39/C39M-12a, while the elastic modulus was measured following the ASTM C469 standard test method. The splitting test was employed to determine the tensile strength [21]. Unlike conventional concrete, for which reliable prediction models are available, the long-term creep and shrinkage behaviour of heat-cured low-calcium fly ash geopolymer concrete—which is a major contributor to its long-term damage—is not yet well established. Therefore, additional dedicated material tests were carried out to characterise its creep and shrinkage properties for use in the numerical analysis.

The geopolymer concrete showed low 28 days compressive strength (<20 MPa) under ambient curing (23 °C, 50 % RH), typical of low calcium fly ash binders [10]. To improve the compressive strength, three heat curing conditions were used.

- 1D-Curing: 80 °C water baths for 1 day.
- 2D-Curing: 80 °C water bath for 2 days.
- 7D-Curing: 80 °C water bath for 7 days.

After casting, specimens were sealed to retain moisture and kept at 40 °C for 24 h before demolding and heat curing. After the curing period, specimens were stored in the laboratory conditions. The material properties are provided in Table 4 versus heat-curing

Table 3
Loads and curing conditions of the conventional concrete beam.

Beam	Pre-cracking peak load	% of SYL	Wet Curing	Sustained load	% of SYL
B1	70 kN	38 %	28 Days	0	0 %
B2	70 kN	38 %	28 Days	40 kN	22 %
B3	90 kN	50 %	28 Days	90 kN	50 %
B5	60 kN	33 %	7 Days	40 kN	22 %
B6	70 kN	38 %	7 Days	70 kN	38 %

*SYL = Steel Yielding Load.

Table 4
Mechanical properties of geopolymer concrete versus heat curing duration.

	Ambient	1D80	2D80	7D80
f_{cm28} (MPa)	18.7	43.5	48.0	54.5
E_{cm28} (GPa)	18.0	20.3	23.7	22.0
f_{tm28} (MPa)	2.3	3.6	3.9	4.5

condition.

The aggregate contents listed in Table 5 correspond to the saturated surface dry (SSD) condition. The triple aluminosilicate blend was first mixed in the dry state with all aggregates for approximately 3 min. Subsequently, the alkaline activator solution was gradually introduced, followed by the addition of free water. Both the concrete cylinders prepared for mechanical testing and the beam specimens were compacted using a poker vibrator to ensure adequate consolidation. The workability of the fresh concrete was evaluated using the standard slump test, yielding a slump value of 130 mm.

The GPC specimens were heat-cured at 80 °C for 24 h immediately after casting. This curing regime is critical for accelerating the geopolymerization reaction, enhancing early strength development, and improving the long-term stability of the aluminosilicate gel network. As reported in previous studies [15,21,25].

The tested beams measured 2450 mm in total length, with a span of 2250 mm between supports and a cross-section of 250 mm × 120 mm. The reinforcement layout is illustrated in Fig. 7 Each beam was reinforced with two longitudinal steel bars of 16 mm diameter (N16), complying with Australian standards, and a concrete cover of 14 mm. Shear reinforcement was provided using stirrups spaced at 200 mm intervals. The longitudinal reinforcement steel exhibited a characteristic yield stress (f_y) of 500 MPa.

Pre-cracking test: Beams pre-cracking was conducted at 28 days, all beams underwent pre-cracking by applying loads of either 50 kN or 70 kN including loading cycles, as detailed in Table 6. The maximum load applied was ranging from 50 % to 70 % of the Steel Yield Load (SYL) measured at 100 kN [21], which were higher values than for the conventional concrete beams (Table 3). During this phase, the deflection and cracks formation were meticulously recorded. The instantaneous stiffness of the cracked beams was assessed during the loading cycles, defined as short-term stiffness.

Long-term Sustained Load Test: After pre-cracking, the beams were subjected to a sustained load of 40 kN for 120 days, except for one beam, which was left unloaded (beyond self-weight) to evaluate the shrinkage effects with minimal loading influence. The sustained load was maintained using a spring-loading device, ensuring consistent loading despite potential creep, cracking-induced stiffness loss, and gradual reduction in tension stiffening over time. Throughout the test period, the progression of cracking and the increase in deflection were monitored to assess the time-dependent effects of creep and shrinkage. Following the sustained loading period, the reinforced concrete beams are subjected to the same loading cycles as the ones used for the pre-cracking test to assess the stiffness reduction due to long term effects, define as long-term stiffness.

In addition, shrinkage tests were conducted on 75 × 75 × 300 mm prisms, following Australian Standard AS1012.13 (1992). Following the heat curing period, the specimens were stored in a controlled environment with a temperature of 23 °C and relative humidity of 50 %. The total shrinkage was measured post heat-curing and up to 90 days.

Creep tests were performed on cylindrical specimens (100 mm diameter, 200 mm height) in accordance with Australian Standard AS1012.16 (1996). These tests began at 28 days after casting, processing the heat-curing period, then with a sustained load equivalent to 40 % of the 28-day compressive strength applied. For each curing condition, three specimens were tested over a 90-day period. The results of both shrinkage and creep tests were compared with predictions for equivalent OPC-based concrete beam, calculated using Eurocode 2 (EN 1992-1-1, 2004). The creep and shrinkage test results are presented in Fig. 8, showing that heat-cured low calcium fly ash geopolymer concrete shrinkage and creep are significantly lower than standard predictions. Depending on the heat curing regime, the creep coefficient is 70 %–80 % lower than the calculated values using Eurocode 2.

4. Comparison between experimental results and simulations

4.1. Case 1: conventional concrete beams analysis

For conventional concrete beam, the material-level creep and shrinkage data were not available. Therefore, the AS3600 creep and

Table 5
Low calcium fly ash geopolymer concrete mix design.

Material	(kg/m^3)
Coarse aggregate	1138
Fine aggregate	730
FA	200
Kaolite HPA	55
GGBFS	45
Sodium hydroxide solution (NaOH)	45.7
Sodium silicate solution (Na_2SiO_3)	114.3
Free water	31

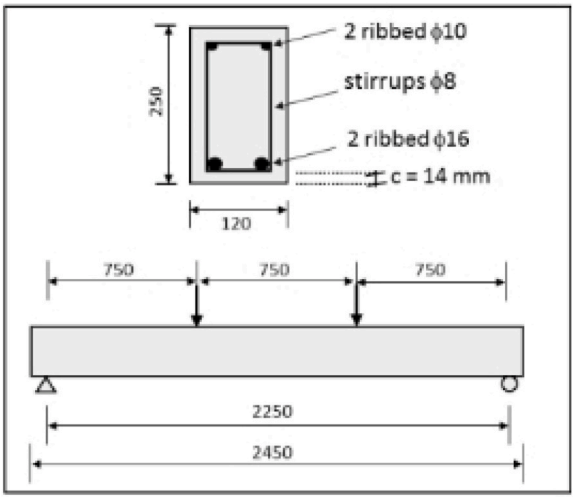


Fig. 7. Design of the geopolymer concrete beam.

Table 6
Loads and curing conditions of the geopolymer concrete beam.

Beam	Pre-cracking maximum load	% of SYL[a]	Curing	Sustained load	% of SYL
B1	70 kN	70 %	7D80	40 kN	40 %
B2	50 kN	50 %	7D80	40 kN	40 %
B3	50 kN	50 %	2D80	Self-weight loading	0 %
B4	50 kN	50 %	2D80	40 kN	40 %
B5	50 kN	50 %	1D80	40 kN	40 %

[a] SYL = Steel yielding load.

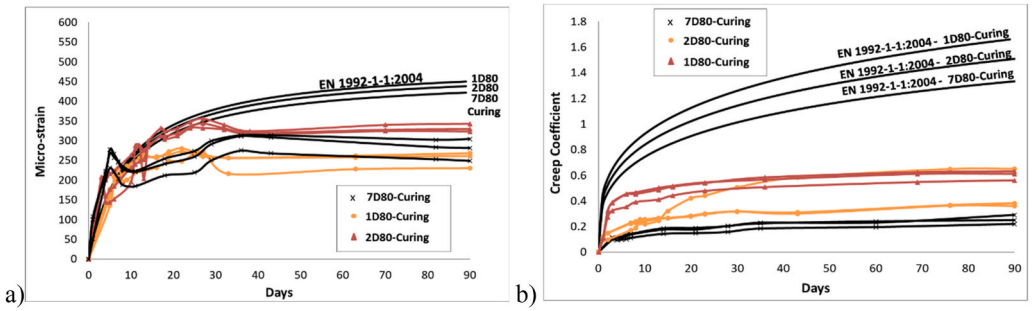


Fig. 8. a) Total shrinkage strain b) creep coefficient obtained for all curing conditions and all concrete specimens.

shrinkage models were implemented via a user subroutine in ABAQUS to represent the time-dependent behaviour of concrete. The concrete beam was modelled by C3D8 elements, and the steel bars were modelled by T3D2 elements. The parameters setting was provided in section 2. The mesh size for concrete was 15–30 mm. Fig. 9 shows the design of the concrete beam FE mesh.

In the numerical simulation, the beam was modelled as a simply supported member. The boundary conditions were applied by constraining one end as a pinned support and the other end as a roller support

A four-point bending configuration was adopted to reproduce the experimental loading scheme. Two concentrated loads were applied through reference points located at one-third and two-thirds of the clear span, respectively, generating a constant-moment region between the loading points. The vertical forces at these positions were transferred to the top surface nodes of the beam via kinematic coupling constraints, ensuring uniform load distribution and avoiding localized stress concentrations.

4.1.1. Conventional concrete beams time-dependent deflection under sustained loading

Fig. 10 compares the time-dependent deflection increase under sustained loading measured experimentally to ABAQUS simulation results for conventional reinforced concrete beams B2, B3, B5, and B6. The values of instantaneous deflections reported in Fig. 10 at day 0 are calculated based on the short-term stiffness predicted by the numerical simulations as detailed in section 4.1.2. Fig. 10 shows

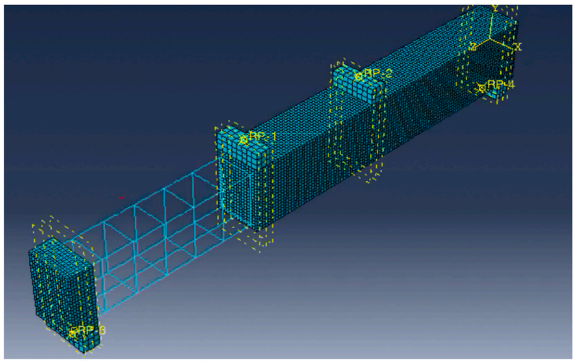


Fig. 9. Finite element model of the conventional concrete beam in ABAQUS.

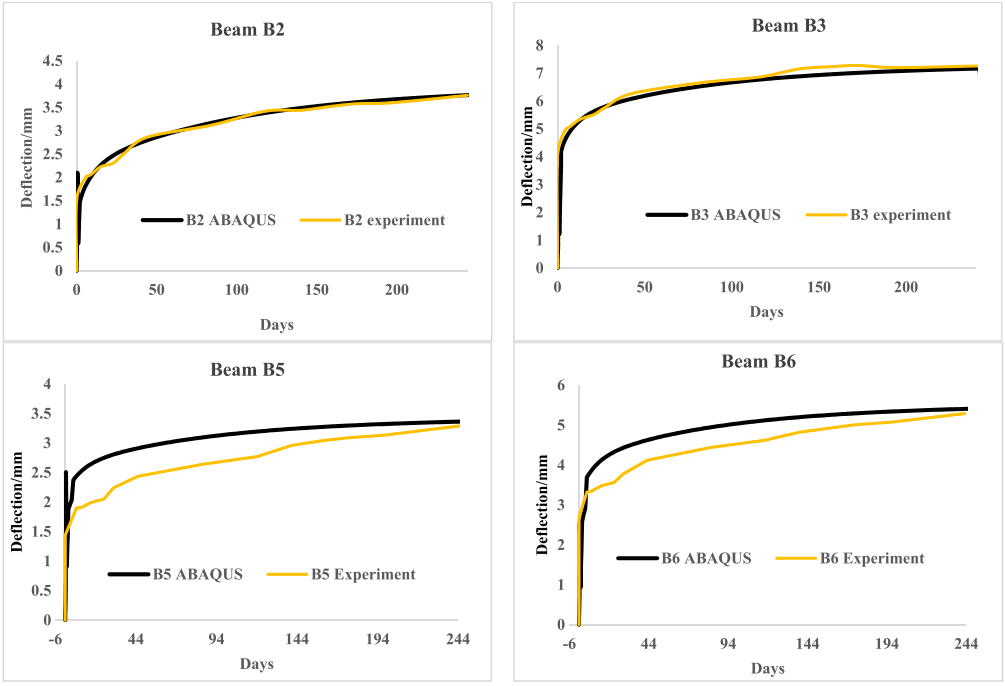


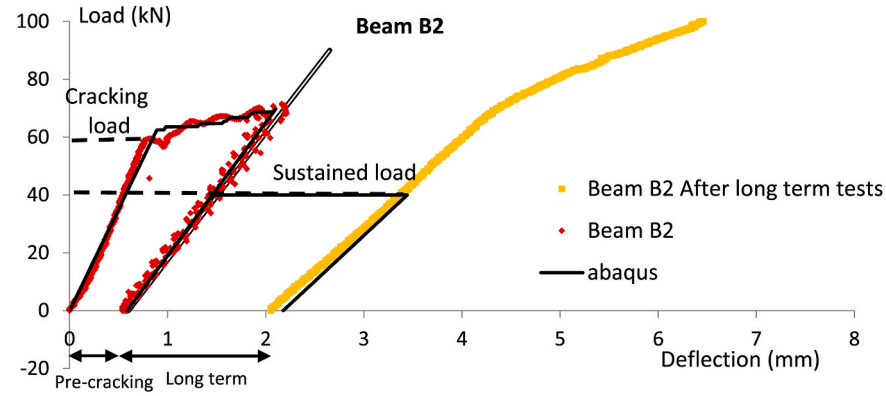
Fig. 10. Long term deflection of the reinforced conventional concrete beams.

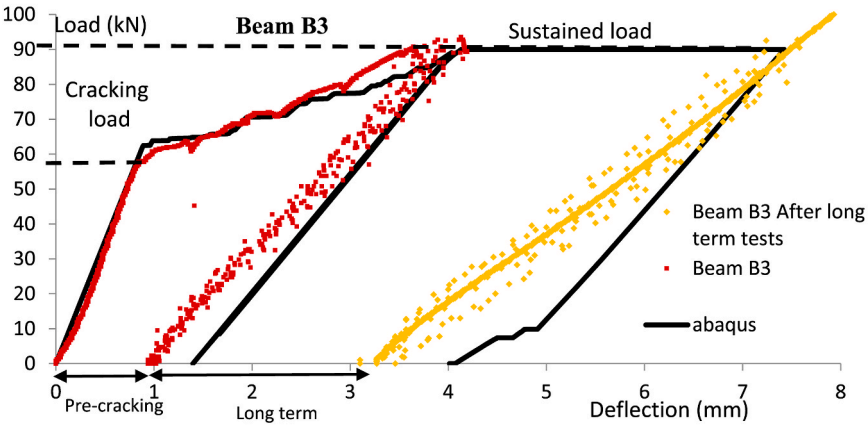
a strong correlation between the model predictions of the time-dependent increase in deflection over about 250 days under sustained loading and the experimental results. The increase in deflection dependents on the sustained load applied. For example, the deflection of beam B3 increased by about 3 mm under 90 kN sustained loading as the deflection of beam B2 increased by only 2 mm under 40 kN sustained loading. This is captured very well by the simulation demonstrating the validity of the finite element model in accounting for the effect of compressive concrete creep in the analysis of the time-dependent serviceability of reinforced concrete beams.

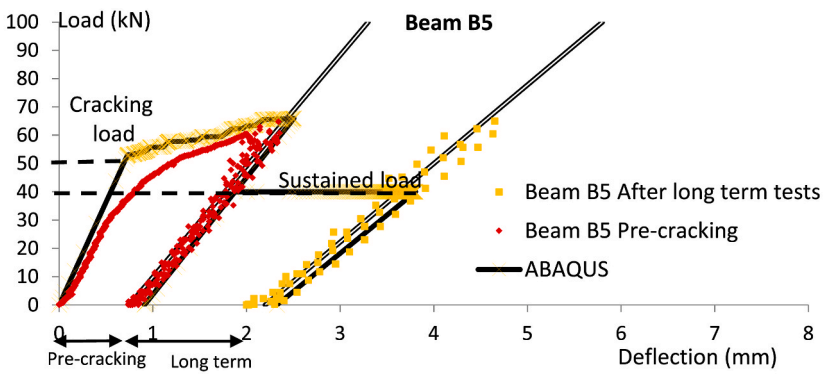
Compared with Beams B2 and B3, the simulated deflection of Beams B5 and B6 shows a relatively larger deviation from the experimental results. This discrepancy is primarily attributed to the inherent randomness of concrete material behaviours. In practice, the creep and shrinkage properties of concrete exhibit considerable scatter even under nominally identical mix proportions and curing conditions, as confirmed by previous long-term experiments. However, in the present finite-element model, the time-dependent deformation is defined deterministically based on the standard formulations and calibrated average parameters. Despite this difference, the overall trend and the order of magnitude of the long-term deflection remain consistent with the experimental observations, confirming the validity of the proposed modelling approach.

4.1.2. Conventional concrete beams load-deflection analysis

The load-deflection response of the concrete beams, subjected to loading cycles applied before (short-term response) and after (long-term response) the sustained loading period of about 250 days, provides crucial insights into their serviceability performance. Fig. 11 presents the results including the whole load history of beams B2, B3, B5, and B6, focusing on cracking load, permanent







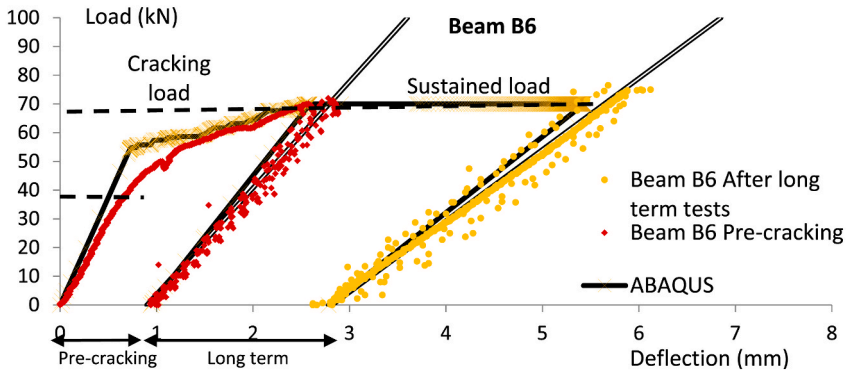


Fig. 11. Load-deflection comparison of Concrete beams (Beam 2 to Beam 6).

deflection due to concrete cracking and time-dependent effects, stiffness before and after the sustained loading period.

In Fig. 11, the first part of the load-deflection response, starting with a deflection equal to zero, is the pre-cracking test when beams are loaded for the first time. The maximum values of the load applied are provided in Table 3 for all beams. When the peak load is reached, beams are unloaded and then loading cycles are performed several times without exceeding the peak load in order to assess the instantaneous (short-term) stiffness of the cracked beams and the permanent residual deflection after unloading due to irreversible damages such as concrete cracks. Then, the effect of the sustained loading period in term of deflection increase is reported. The values of time-dependent deflection under sustained load reported in Fig. 11 are equal to the ones presented in Fig. 10. This leads to a significant shift of the load deflection response labeled "after long term tests" which is obtained following the 250 days of sustained loading period, beams being subjected to the same loading cycles as the one performed during the pre-cracking tests. This load-deflection response allows to assess the reduction in beam stiffness (long-term stiffness) and the additional permanent deflection attributed to the effects of the sustained loading, presented after unloading the beams in Fig. 11.

ABAQUS model predictions are compared to the experimental load-deflection responses in Fig. 11. The numerical simulation was implemented using a three-step loading protocol in Abaqus.

- Pre-cracking loading phase: the beam is loaded up to the experimentally determined target load and unload.
- Sustained loading phase: the load is applied to target sustained load and kept constant over the 250 days of sustained loading period.
- Unloading phase: The applied load was gradually reduced to zero.

The transition between these loading stages was controlled through an amplitude function in Abaqus to ensure accurate representation of the load history.

Cracking load: The identification of the cracking load was primarily based on a noticeable reduction in beam stiffness, which became evident in the response curves. As expected, the cracking load is higher for beams B2 and B3 than for B5 and B6. This is because B2, and B3 were continuously moist cured for the 28-day period before the load tests were performed, and B5 and B6 underwent significant shrinkage prior to first loading. The cracking load of both B2 and B3 was ranging from 55 to 60 kN exhibiting strong agreement with the model predictions calculated using a flexural tensile stress equal to the concrete tension strength of 3.5 MPa. This tensile strength was obtained from the flexural test on concrete prisms and was subsequently used as the equivalent tensile strength parameter in the CDP model.

For the beams B5 and B6, that were moist cured for only seven days, the cracking load was significantly reduced as a result of both the modification to the concrete hydration process (i.e., the slower strength gain) and the restraint to drying shrinkage provided by the reinforcement, creating tensile stress in concrete prior to first loading. Effects that were not accounted for in the modelling.

Short-term beam stiffness and permanent deflection: The overall behaviour during the loading cycles is linear elastic, allowing to determine the short-term stiffness of the cracked beams. As expected, the short-term stiffness decreases with increasing peak load because the stiffness is affected by the number of flexural cracks along the span and by the steel-concrete interface damage associated with increasing applied loading. The short-term stiffness predicted by the numerical simulations were very accurate for beams B2, B5 and B6. The peak load applied was ranging from to 60 kN–70 kN for these beams, corresponding to about 33 %–38 % of the load leading steel reinforcement to yield (SYL = 180 kN). The concrete damage properties and concrete behaviour for uniaxial tension, presented in Table 2 and Fig. 5 respectively, seem to be appropriately calibrated to predict the instantaneous stiffness of cracked reinforced concrete beams subjected to moderate loading consistent with standard service loads. However, in the case of Beam B3, with a peak load of 90 kN (50 % of the SYL), the model prediction is significantly over-estimating the cracked beam stiffness. This is due to additional concrete damage at the steel-concrete interface impacting the transfer of tensile stress from steel to concrete. The resulting loss in concrete tension stiffening leads to a further reduction in stiffness [10] which is not accounted for by the model proposed in this study.

The permanent deflection on unloading after the short-term tests ranged between 0.5 and 1 mm, depending on the maximum load applied, and was caused by irreversible damage relating to concrete cracking. The calculated values of permanent deflection were also in good agreement with experimental values for all beams, except for B3 due to the over-estimated short-term stiffness.

Long-term beam stiffness: After the sustained loading period, for all beams, the long-term stiffness measured by performing the same loading cycles was significantly reduced compared to the value recorded during the pre-cracking tests. Notably, beam B3 exhibited the largest stiffness degradation, being subjected to the highest value of sustained loading. This reduction in stiffness can be related to the modification of the cracking pattern of the beams following the sustained loading period. Depending on the beam, new cracks appeared outside the constant bending moment region, the length of the existing cracks increased, and, in some cases such as B3 subjected to the highest sustained load, new cracks occurred between existing cracks in the constant bending moment zone of concrete. But, this stiffness reduction can also be attributed to the accumulation of micro-cracks and progressive damage within the concrete matrix under sustained loading conditions. ABAQUS model predictions of the long-term beam stiffness are excellent for beams B2, B5 and B6, underlining the necessity of incorporating both concrete viscoelastic behaviour and progressive accumulation of creep-induced damage mechanisms in numerical models to capture long-term structural behaviour accurately. Due to its high sustained load history, B3 long-term stiffness degradation involves additional steel-concrete interfacial damage which are not accounted for in the simulations, as stated previously. It is important to note that the sustained loading of B3 (50 % SYL) is way higher than typical permanent load considered for serviceability design, being within the range of 20 %–25 % of SYL. As a result, the stiffness over-estimation by the model proposed has no practical consequence. The model proposed is accurate within the range of permanent load considered for reinforced concrete serviceability design. The permanent deflections observed after the sustained loading period

were also consistent with model predictions across all beams, except for B3 due to the over-estimated long-term stiffness.

4.1.3. Mesh sensitivity analysis and error analysis

Three graded meshes were evaluated: a coarse mesh with a 30 mm global size transitioning to 5 mm in the refined zone, a medium mesh with 20 mm transitioning to 5 mm, and a fine mesh with 15 mm transitioning to 5 mm, as illustrated in Fig. 12.

Fig. 13 compares the experimentally measured mid-span deflection histories of Beams B2, B3, B5, and B6 with the numerical predictions obtained from the three mesh densities (global element size 30 mm, 20 mm, and 15 mm, all with 5 mm local refinement in critical regions). For all beams, both the experiment and the simulations show a rapid initial increase in deflection within the first few days after loading, followed by a slower, asymptotic growth over approximately 250 days. This trend is consistent with time-dependent deformation governed by early cracking, tensile softening, shrinkage, and sustained-load (creep) effects: most of the flexural region is mobilized shortly after the load application, whereas the subsequent increase in long-term deflection primarily reflects the effect of concrete creep rather than abrupt additional cracking. Among the four beams, B3 and B6 exhibit the largest long-term deflections, which is consistent with their higher sustained bending moment compared to B2 and B5. Beam B2 shows the smallest long-term deflection as it is subjected to the lowest sustained bending moment applied. Beam B6 lies between these two extremes but continues to accumulate measurable deflection throughout the monitoring period. Overall, the finite element (FE) predictions reproduce not only the absolute magnitude of the long-term deflection but also the curvature of the experimental deflection–time trajectory: the numerical curves follow the same "fast-then-slow" growth shape and remain close to the experimental envelope at late ages (100–250 days), when serviceability is most critical.

Fig. 14 summarizes the quantitative accuracy of each mesh level by reporting multiple error metrics for each beam. Five standard error metrics were used for comparison. In the below equations s_i means the simulation deflection results at load point the e_i means the measured deflection at loading time.

$$RMSE = \sqrt{\left(\left(\frac{1}{n}\right)\sum_{i=1}^{n}(s_i - e_i)^2\right)} \tag{29}$$

$$MAE = \left(\frac{1}{n}\right)\sum_{i=1}^{n}|s_i - e_i| \tag{30}$$

$$MBE = \left(\frac{1}{n}\right)\sum_{i=1}^{n}|s_i - e_i| \tag{31}$$

$$|PBIAS| = 100 * \left|\frac{\sum_{i=1}^{n}|s_i - e_i|}{\sum_{i=1}^{n}|e_i|}\right| \tag{32}$$

$$MAPE = 100 * \left(\frac{1}{n}\right) * \sum_{i=1}^{n}\left|\frac{(s_i - e_i)}{e_i}\right| \tag{33}$$

For beams B2 and B6, all three meshes give consistently low errors. Typical RMSE values are on the order of 0.16–0.24 mm, MAE remains below about 0.21 mm, and the percentage bias |PBIAS| is generally below 6 %. This indicates that, for these beams, the model is able to predict the long-term deflection with sub-millimetre absolute accuracy and only a small systematic tendency to overestimate or underestimate. Beam B3 is more mesh-sensitive: the coarsest mesh (30 mm global size) tends to overpredict the deflection over time, which appears as both higher RMSE/MAE (≈0.3 mm) and a larger positive |PBIAS| (~5 %). When the global mesh is refined to 20 mm, the errors drop markedly: RMSE and MAE fall to ~0.15 and ~0.12 mm, respectively, and |PBIAS| is reduced to below 2 %, indicating that the 20 mm mesh can capture the stiffness degradation under higher sustained load without systematically inflating the creep deflection. Beam B5 shows the largest absolute and relative errors across all meshes (e.g. RMSE up to ~0.44 mm and |PBIAS| exceeding 10 %). Although B5 was subjected to a lower sustained load level than B6, the discrepancy cannot be attributed to load-induced bond deterioration but rather to modelling uncertainty in the time-dependent parameters assigned to this beam. In particular, a slight overestimation of shrinkage and creep in the early stage was carried forward in the time-dependent analysis and accumulated over the

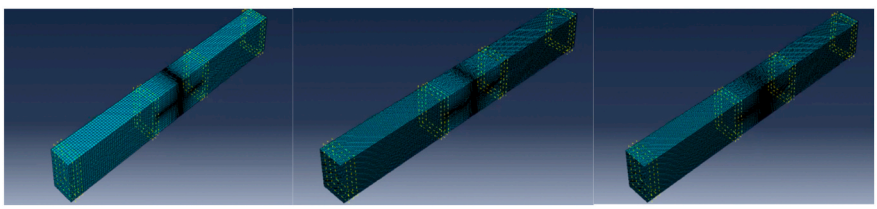


Fig. 12. Different global mesh size from 30 (left), 20 (middle), 15 (right).

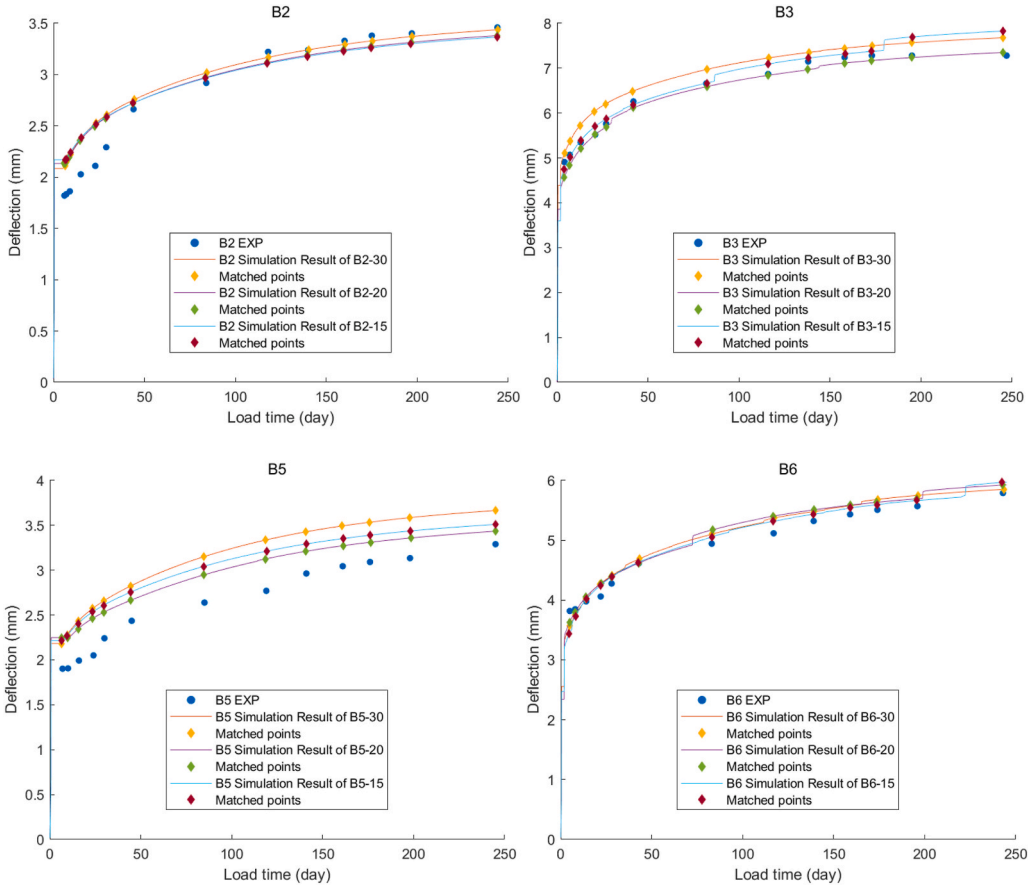


Fig. 13. Time-dependent deflection results of mesh sensitivity analysis.

simulation period, which explains the larger deviation from the experimental curve even though the deflections of the two eventually become comparable at the last observation day. It should also be noted that, even for concrete with the same mix and curing conditions, shrinkage and creep behaviours exhibit an inherent scatter, so a deterministic set of time-dependent parameters cannot fully capture beam-to-beam variability. Even in that case, refining the mesh from 30 mm to 20 mm significantly reduces both amplitude error (RMSE, MAE) and bias (|PBIAS|), although further refinement to 15 mm does not continue to improve the prediction.

4.2. Case 2: heat-cured low calcium geopolymer concrete beam analysis

In this simulation, the creep coefficient and shrinkage data were derived from experimental measurements. The geopolymer concrete beam was modelled using C3D8 elements for the concrete, while T3D2 elements were employed to represent the reinforcing steel bars. Details regarding the materials' parameter settings are provided in Section 2. This FEM analysis specifically focused on Beam 5, which underwent a heat curing regime of 1 day at 80 °C (1D80) and was subjected to a sustained load of 40 kN. Beam 5 was chosen based on its short curing period, which allowed for an evaluation of the structural performance under suboptimal curing conditions. The reinforcement was modelled with an embedded region approach to accurately simulate the interaction between the steel and concrete. The mesh size for the concrete elements was set to 10–30 mm to ensure computational efficiency while maintaining model accuracy. The mesh design for the geopolymer concrete beam is illustrated in Fig. 15. The boundary conditions are same as for the conventional concrete beam simulations.

Fig. 16 presents the fitted curve of the creep coefficient and shrinkage of the of 1 day cured geopolymer concrete at 80 °C (1D80). The experimental data for the creep coefficient covers a period of 90 days, during which the creep strain rate stabilized. For structural simulations extending beyond 90 days, it was assumed that the creep coefficient remained constant until 300 days, reflecting the stabilized behaviour observed in the experimental results.

4.2.1. Geopolymer concrete beam time-dependent deflection under sustained loading

Fig. 17 **compares the time-dependent deflection increase under sustained loading measured experimentally to ABAQUS simulation results for geopolymer rei**nforced concrete beams B5. The value of instantaneous deflections reported at day 0 is calculated based on the short-term stiffness predicted by the numerical simulations as detailed in section 4.2.2.

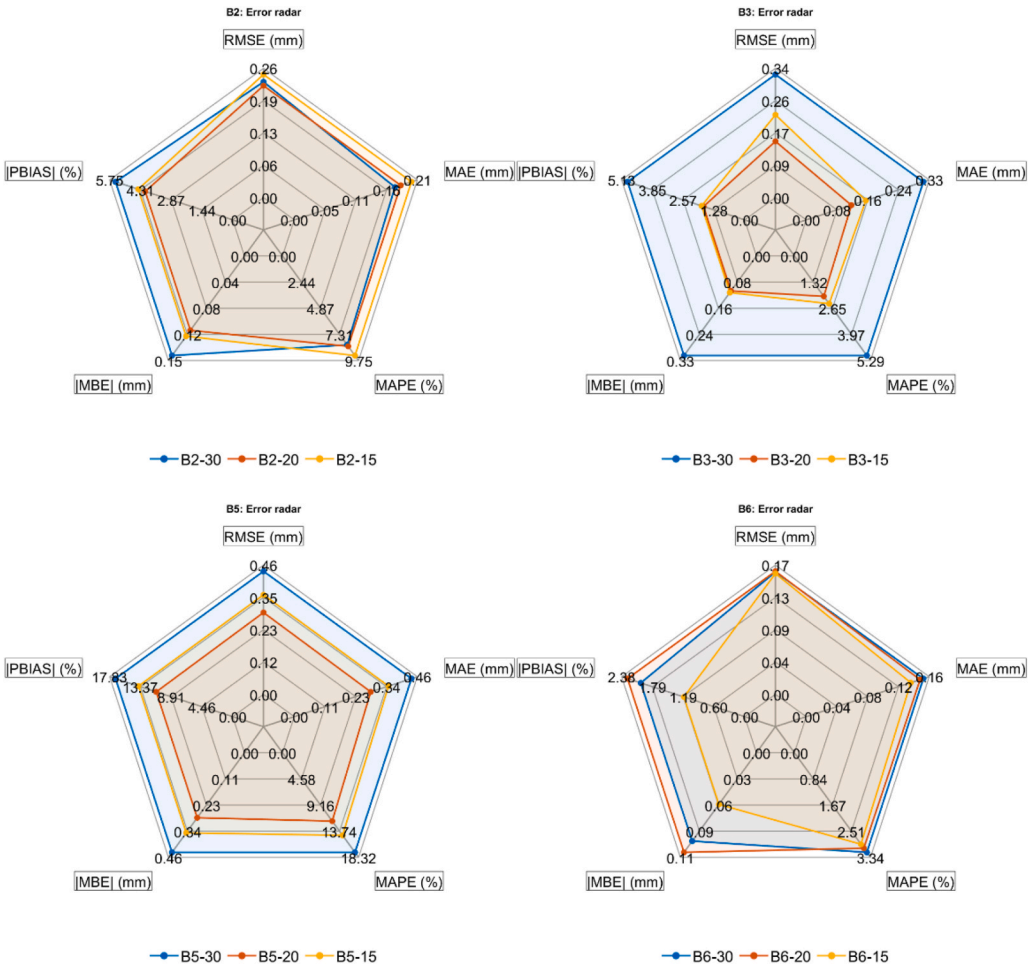


Fig. 14. Error comparison of the different meshes.

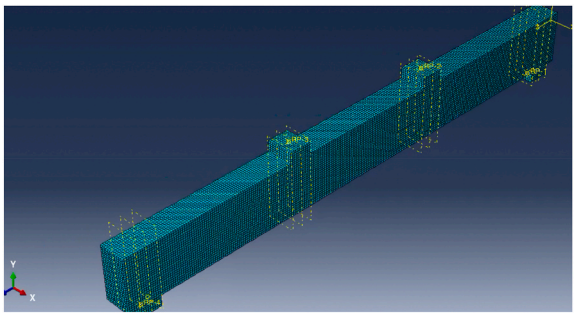


Fig. 15. Finite element model of geopolymer concrete beams in ABAQUS.

The findings show a strong correlation between the numerical simulation and experimental results. Noticeably, the time-dependent deflection increase after 120 days under sustained loading is extremely low compared to the ones of the conventional concrete beams considered in the simulations reported in section 4.1. This is obviously due to the very low creep coefficient of the 1-day heat cured low calcium fly ash concrete. The creep coefficient was about 70 % lower than the one calculated using Eurocode 2 model, demonstrating the validity of the finite element model in capturing the influence of compressive concrete creep on the long-term behaviour of reinforced concrete beams.

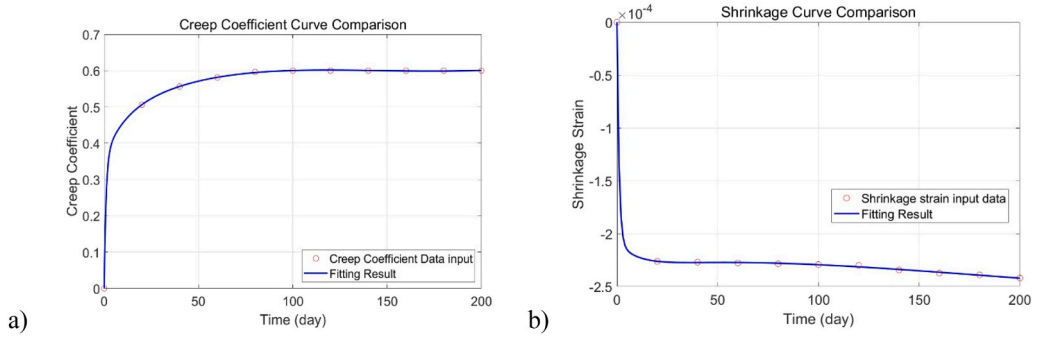


Fig. 16. (a) Dirichlet series fitting curve for Creep coefficient (b)Dirichlet series fitting curve for shrinkage strain.

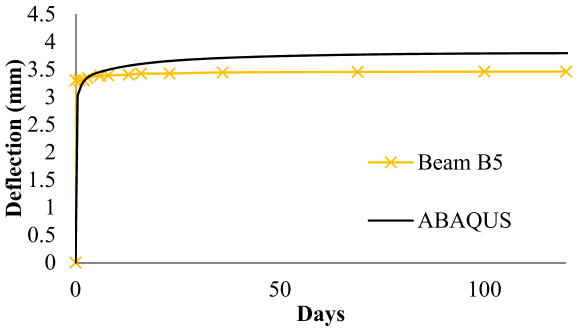


Fig. 17. Geopolymer Concrete beam B5 time-dependent deflection under sustained loading.

4.2.2. Geopolymer concrete beam load-deflection analysis

The loading sequences including load cycles and sustained loading period are similar to the ones adopted for the conventional reinforced concrete beams (see section 4.1). The values of the peak load and the value and duration of the sustained loading are provided in Table 6 and Fig. 18. In Fig. 18, the cracking load (P_{cr}) was clearly identifiable on the load-deflection curve, model prediction aligning with the experimental observations. For short-term tests (pre-cracking test), the overall behaviour during the loading cycles is linear elastic, similar to the behaviour of the conventional reinforced concrete beams. The short-term stiffness of geopolymer beam B5 was accurately predicted by the numerical simulations. The permanent deflection following the pre-cracking test was also correctly predicted. It appears that the concrete damage properties and concrete behaviour for uniaxial tension, presented in Table 2 and Fig. 5 respectively, calibrated for conventional concrete, are suitable for short-term analysis of heat-cured low calcium fly ash reinforced concrete beams serviceability.

After the sustained loading period, the response of the geopolymer beam under the load cycles is drastically different to that of the conventional concrete beams considered in Section 4.1. Indeed, almost no stiffness reduction was experimentally recorded following the sustained loading period. This was observed for all the heat-cured geopolymer beams tested [21]. As stated in Section 4.1.2 relating to conventional reinforced concrete beams, the decay in stiffness due to the sustained loading period is governed by the concrete viscoelastic behaviour and progressive accumulation of creep-induced damage mechanisms. The graph also shows that the beam stiffness exhibits little degradation following the sustained loading period, and this behaviour is also captured by the model. Due to the extremely low creep coefficient of the heat-cured geopolymer concrete considered, it appears that the magnitude of these time-dependent effects is very limited which can explain this only marginal reduction in stiffness. This is perfectly well captured by the time-dependent numerical analysis proposed. The permanent deflections measured before and after the sustained loading phase were also consistent with the model predictions.

This study highlights the superior stiffness retention and long-term performance of heat cured low calcium fly ash geopolymer concrete. These findings emphasize the potential of this type of geopolymer concrete as a sustainable and high-performance alternative to OPC concrete particularly for precast applications where heat-curing is common practice. The overall agreement between simulation and experimental results also validates the predictive capability of the simulation model for assessing long-term serviceability behaviour.

4.2.3. Mesh sensitivity analysis and error analysis

All simulations used identical material parameters, boundary conditions, step controls and local refinement near the supports and the load application region. Only the global element size was varied, yielding three graded meshes showed in Fig. 19, there are coarse 30 mm, medium 20 mm, and fine 10 mm for the mesh sensitivity analysis.

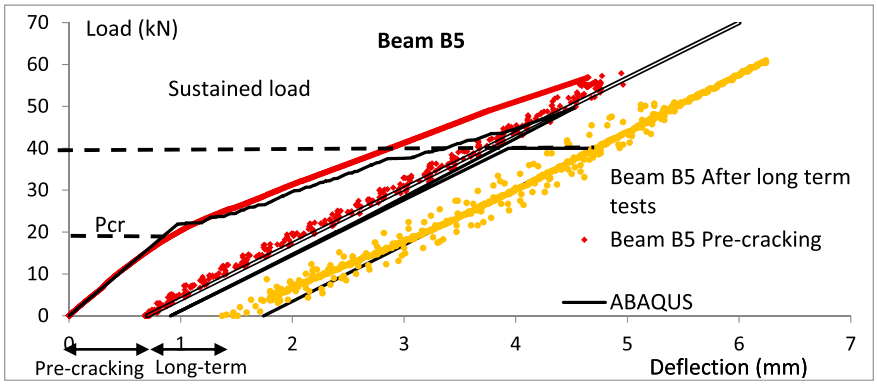


Fig. 18. Geopolymer concrete beam load-deflection response.

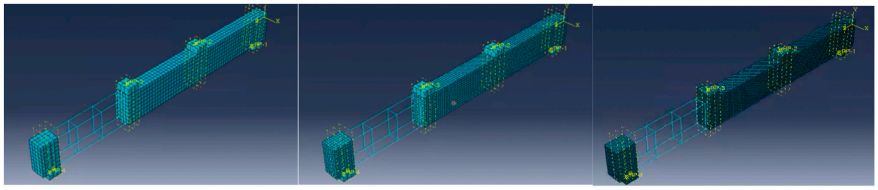


Fig. 19. Mesh sensitivity analysis for Geopolymer concrete.

Fig. 20 shows that, for the geopolymer concrete beam, the creep induced deflection increase under sustained loading happen mostly over the first 20 days, followed by only a very modest additional increase over the remainder of the observation period. Then, the deflection–time curve tends to flatten, indicating limited further creep-driven deformation.

The deflections measured experimentally were compared to the simulated values by linear interpolation at the same time instants (the "matched points" marked in Fig. 20). The error analysis confirms that the deflection overestimation is mesh dependent (Fig. 21). The coarsest mesh (30 mm global size) overestimates the test results the most, with absolute errors on the order of half a millimetre and a relative bias of about 11.05 %, showing a consistent tendency to overpredict long-term deflection. Refining the global mesh to 20 mm reduces the error roughly by half, but a noticeable upward bias remains. Only the finest mesh (10 mm global size) brings the error down to about one tenth of a millimetre and reduces the percentage error to below roughly 6 %, indicating that both the amplitude and the systematic bias are substantially controlled at that resolution.

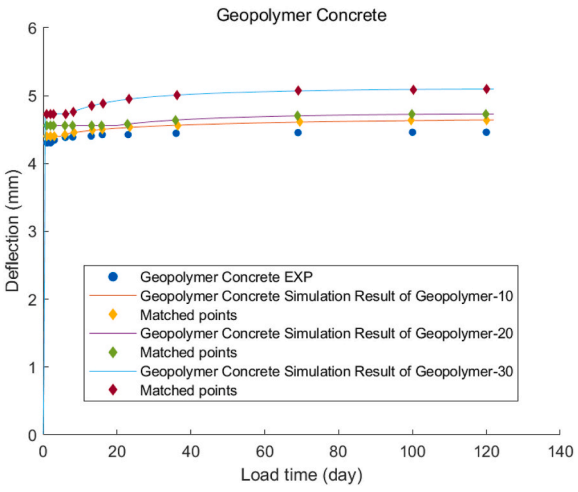


Fig. 20. Mesh sensitiveness analysis result of Geopolymer concrete beam.

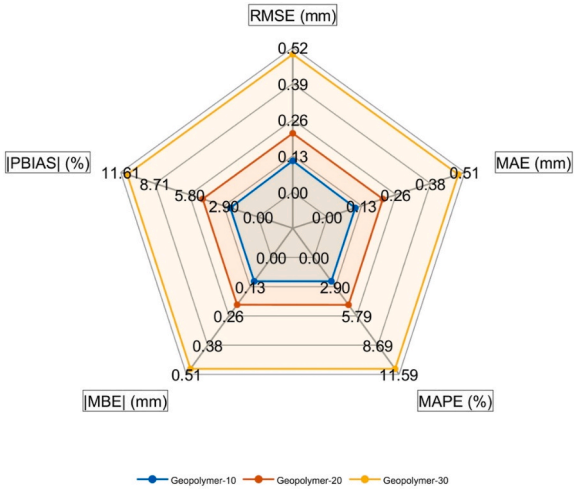


Fig. 21. Error results of Geopolymer concrete beam.

4.3. Damage comparison between conventional concrete and geopolymer concrete beams

Fig. 22 shows the experimental cracking pattern of the conventional concrete beam B6. Figs. 23 and 24 illustrate the tensile damage (DAMAGET) distribution in conventional concrete beam B6 at two different loading stages: (a) Step-1 at 1 day and (b) Step-2 at 244 days. The meshes size are refined here to get a clearer display of the damage distribution. The variable ranges from 0 (undamaged) to 1 (fully degraded), indicating the extent of material stiffness loss due to damage. At 1 day, following the pre-cracking loading test simulation, damage is observed in the tension zone at the bottom of the beam, characterized by scattered vertical small cracks and main flexural cracks with about 200 mm average spacing, being consistent with experimental observations showed in Fig. 22 [26].

As the beam undergoes long-term sustained loading (244 days), the tensile damage distribution shows a clear increase in damage magnitude, propagation of existing main cracks and extension of the damage zone toward the supports. This indicates a progressive accumulation of tensile damage over time. The damage pattern evolution aligns well with experimental observations. This confirms the model's ability to realistically capture the time-dependent degradation behaviour of conventional concrete under sustained service load conditions.

Figs. 25 and 26 present the scalar stiffness degradation variable (SDEG) of the geopolymer concrete beam at Day 1 and Day 150, respectively. At Day 1 (Fig. 25), following the pre-cracking loading test simulation, the SDEG distribution is similar to the one observed in the case of the conventional concrete beam. Damage is localized along the tensile zone at the bottom of the beam. Main flexural cracks with about 150 mm average spacing formed, being consistent with experimental observations. By Day 150 (Fig. 26), although a slight increase in SDEG values can be noticed, the damage distribution after 150 days under sustained loading is very close to the one observed before the sustained loading period. This explains why the numerical analysis of the geopolymer concrete beam led to only a marginal stiffness degradation under sustained loading over time, which is consistent with the experimental findings. The simulation highlights the favourable long-term damage resistance of geopolymer concrete, particularly in resisting tensile stiffness loss, due to the



Fig. 22. Observed cracking pattern of the conventional beam B6.

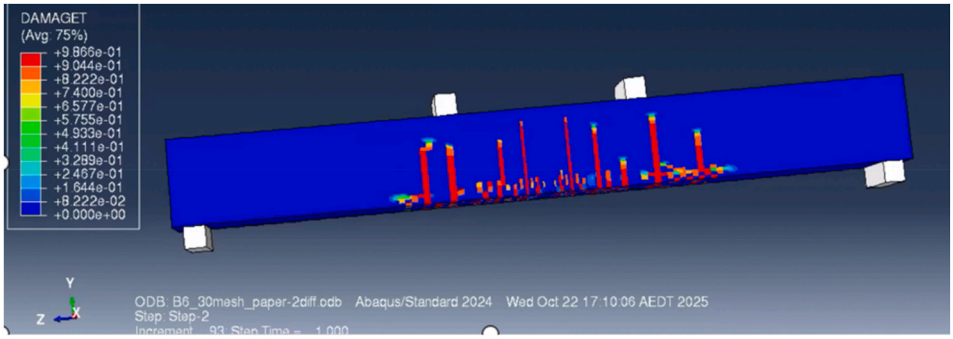


Fig. 23. Day 1 tensile damage condition of conventional concrete beam B6.

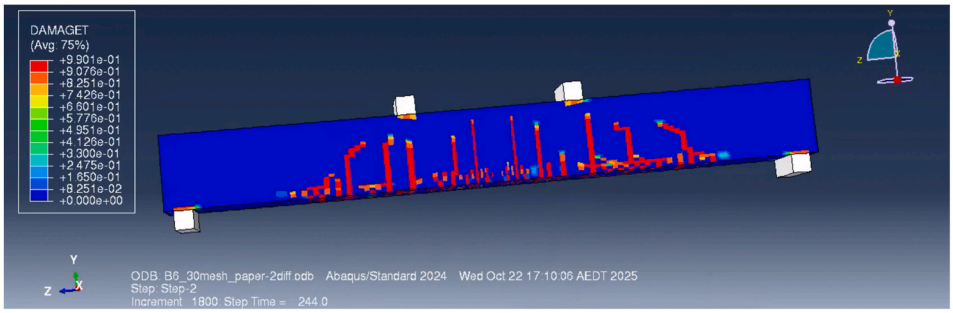


Fig. 24. Day 244 tensile damage condition of conventional concrete beam B6.

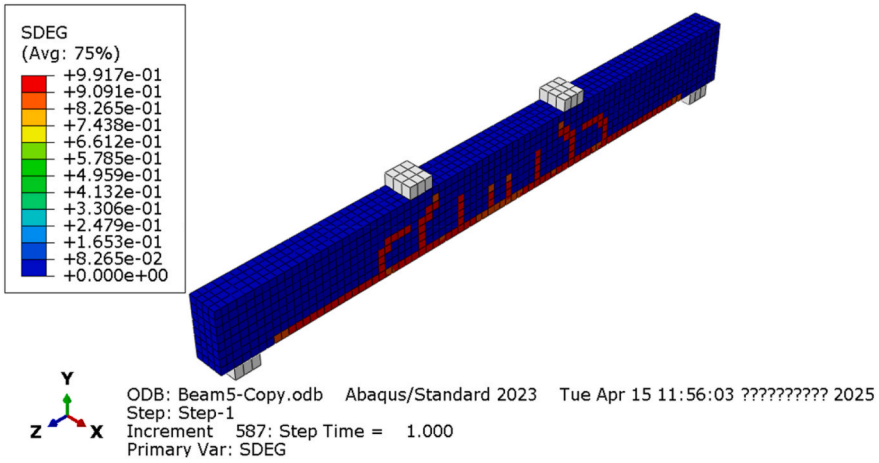


Fig. 25. Day 1 damage condition of the Geopolymer concrete beam.

low creep and shrinkage of heat-cured geopolymer concrete.

4.4. Stiffness degradation of beams

The stiffness reduction can be calculated using the following equation. In the equation, the K_i is the initial stiffness of the concrete beam after the pre-crack test, and the K_t is the stiffness of the concrete beam after the long-term test.

$$K_r = \left(1 - \frac{K_i}{K_t}\right) * 100\% \tag{34}$$

Fig. 27 compares the stiffness reduction percentages between simulation and experimental results for different types of concrete beams, including ordinary Portland cement (OPC) concrete and geopolymer concrete. The OPC concrete beams (B2, B5, B6, B3)

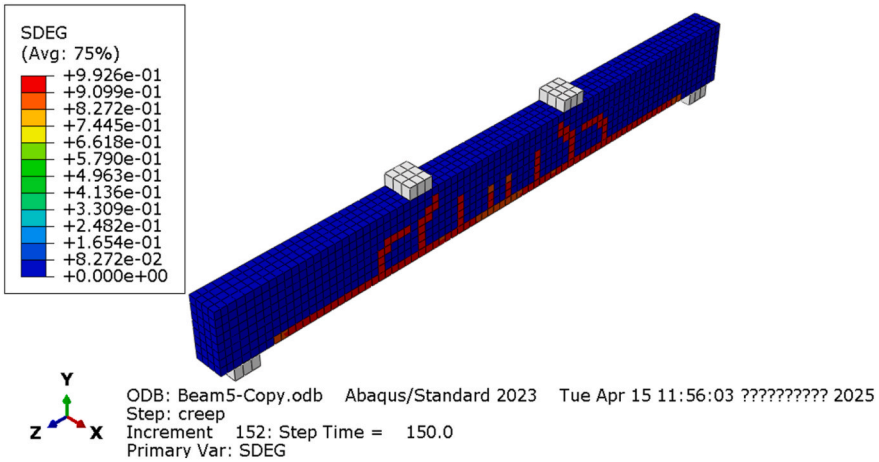


Fig. 26. Day 150 tensile damage condition of the Geopolymer concrete beam.

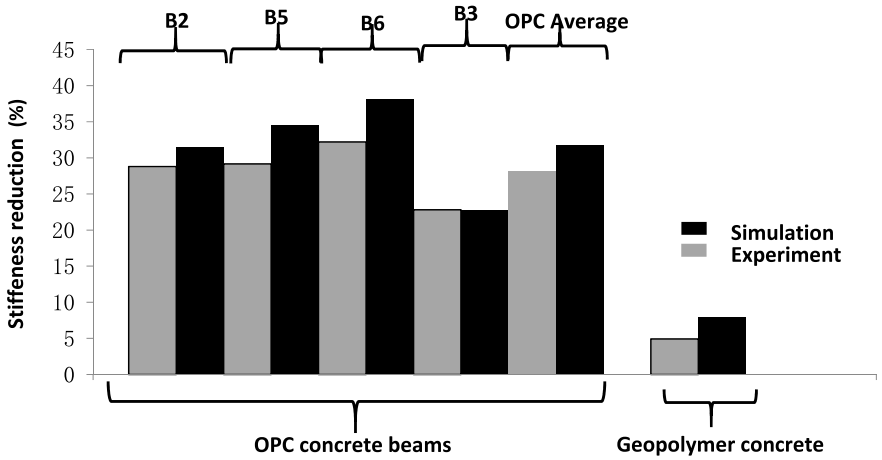


Fig. 27. Stiffness degradation comparison of the beams.

exhibited stiffness reductions ranging from 25 % to 40 %, with B6 showing the highest reduction and B3 the lowest. On average, the simulation results align well with experimental data, effectively capturing the long-term stiffness degradation of OPC concrete beams.

In contrast, the geopolymer concrete demonstrated a very low stiffness reduction, with simulation and experimental results being in close agreement. This highlights the superior stiffness retention and long-term performance of geopolymer concrete, which is likely attributed to its unique material properties, such as low creep and low shrinkage. These findings emphasize the potential of geopolymer concrete as a sustainable and high-performance alternative to OPC concrete. The overall agreement between simulation and experimental results also validates the predictive capability of the simulation model for assessing long-term structural behaviour.

5. Conclusions

This study developed a comprehensive numerical framework integrating a stepwise creep and shrinkage analysis user-defined subroutine in ABAQUS allowing to capture the time-dependent deformations and stiffness evolution of cracked reinforced concrete beams under service loading. The finite element model successfully simulated both long-term stiffness degradation and time-dependent deflection increase under sustained loadings. Both conventional and heat-cured low calcium fly ash reinforced concrete beams were successfully simulated under service loading.

For conventional concrete beams, the deflection prediction error between simulation and experiments was within 4 % for loading values consistent with the practical range of permanent load considered for reinforced concrete serviceability design, validating the accuracy of the numerical model. For the heat-cured geopolymer concrete beam, the deflection prediction error was within 2.4 %, confirming that the developed model can also effectively predict the long-term serviceability of heat-cured low calcium fly ash geopolymer concrete structures. The simulation results emphasize the importance of incorporating both creep and damage mechanisms in the numerical modelling to predict the long-term serviceability accurately.

This study highlights the superior long-term performance of heat-cured low calcium geopolymer concrete structures, characterized by a minimal stiffness degradation and enhanced structural integrity under sustained loading, highlighting geopolymer concrete's potential as a sustainable and high-performance alternative to Ordinary Portland Cement (OPC) concrete, particularly for precast applications where heat-curing is common practice.

The mesh-sensitivity study shows that, for the conventional reinforced concrete beams, the FE model can accurately reproduce the long-term mid-span deflection under sustained load using a global mesh size of about 20 mm (with local refinement). At this mesh level, the predictions match the experiments within a few tenths of a millimetre and the bias is small. Further refinement to 15 mm only gives minor improvement.

For the geopolymer concrete beam, the long-term deflection increase being smaller and more stable than for conventional concrete over time, even a small numerical offset becomes important. The coarse (30 mm) and medium (20 mm) meshes overestimate the sustained deflection. For the 30 mm mesh the overprediction is 0.48 mm, corresponding to an PBIAS of 11 %; for the 20 mm mesh the error is 0.21 mm on average (PBIAS 4.7 %). The fine mesh (10 mm) reduces the error to 0.11 mm and keeps the PBIAS at 2.4 %. As a result, the same modelling approach is suitable for both conventional concrete and geopolymer concrete, but the required mesh density is not the same: ~20 mm is generally sufficient for normal concrete beams, while geopolymer concrete needs a finer global mesh to reach the same level of accuracy.

While the study provides valuable insights into the behaviour of heat-cured geopolymer concrete, additional research is required to develop more accurate material models explicitly tailored for these materials particularly relating to creep and shrinkage. This research validates the proposed numerical approach and establishes a foundation for improving the accuracy and efficiency of creep and shrinkage simulations in concrete structures serviceability. Future work should incorporate environmental factors such as temperature and humidity effects, which are also major factors contributing to concrete cracking, and develop advanced constitutive models to further enhance the predictive capabilities of finite element simulations, such as developing time-dependent constitutive models that explicitly incorporate subcritical damage growth under sustained loading. Additionally, uncertainties in material damage remain a challenge in both creep and instantaneous analysis, which may introduce discrepancies in FEM predictions and should be addressed in future studies.

CRediT authorship contribution statement

Yuan Dong: Writing – review & editing, Writing – original draft, Methodology, Investigation, Formal analysis, Data curation, Conceptualization. **Jun Li:** Writing – review & editing, Writing – original draft, Supervision, Investigation, Formal analysis, Data curation, Conceptualization. **Shami Nejadi:** Writing – review & editing, Writing – original draft, Supervision. **Tengfei Xu:** Writing – review & editing, Writing – original draft, Supervision, Methodology, Investigation, Formal analysis, Conceptualization. **Arnaud Castel:** Writing – review & editing, Writing – original draft, Supervision, Resources, Methodology, Funding acquisition, Data curation, Conceptualization.

Declaration of competing interest

The authors declare that they have no known competing financial interests or personal relationships that could have appeared to influence the work reported in this paper.

Acknowledgement

This research was funded by BG&E and the Cooperative Research Centre (CRC) SmartCrete Project "Refining Design Deformation Predictions by Improving Concrete Volume Stability Assessment (22.PP.0151)".

Data availability

The data that has been used is confidential.

References

[1] Z.P. Bažant, M.H. Hubler, Q. Yu, Damage in prestressed concrete structures due to creep and shrinkage of concrete, in: Handbook of Damage Mechanics, Springer, New York, 2015, pp. 515–564, https://doi.org/10.1007/978-1-4614-5589-9_49.
[2] V. Gribniak, G. Kaklauskas, D. Bacinskas, State-of-art review of shrinkage effect on cracking and deformations of concrete bridge elements, Baltic J. Road Bridge Eng. 2 (4) (2007) 183–193.
[3] Z.P. Bažant, Prediction of concrete creep and shrinkage: past, present and future, Nucl. Eng. Des. 203 (1) (2001) 27–38, https://doi.org/10.1016/S0029-5493(00)00299-5.
[4] Z.P. Bazant, F.H. Wittmann, Creep and shrinkage in concrete structures. https://doi.org/10.1002/zamm.19840640703, 1982.
[5] R.I. Gilbert, Control of flexural cracking in reinforced concrete, ACI Struct. J. 105 (3) (2008) 301–307, https://doi.org/10.14359/19789.
[6] S. Li, Y. Yang, Q. Pu, D. Yang, B. Sun, X. Li, Three-dimensional nonlinear creep and shrinkage effects of a long-span prestressed concrete box girder bridge, Struct. Concr. 20 (2) (2019) 638–649, https://doi.org/10.1002/suco.201800148.
[7] H. Huang, Y. Zhong, C. Yang, M. Chen, A. Wang, J. Chen, H. Zhuang, Y. Wang, Experimental study and prediction model analysis for creep behaviour of recycled ceramic aggregate concrete-filled square-shaped steel tube, Structures 75 (2025) 108674, https://doi.org/10.1016/j.istruc.2025.108674.
[8] Li Faxiong, Spatial Stress Behavior and Variable Effects of Composite Girder cable-stayed Bridges, Doctoral dissertation, Tsinghua University, Beijing, 2011.

[9] Q. Wang, J.L. Le, X. Ren, Numerical modeling of delayed damage and failure of concrete structures under sustained loading, Eng. Struct. 252 (2022) 113568, https://doi.org/10.1016/j.engstruct.2021.113568.
[10] A. Castel, R.I. Gilbert, G. Ranzi, Instantaneous stiffness of cracked reinforced concrete including steel-concrete interface damage and long-term effects, J. Struct. Eng. 140 (6) (2014), https://doi.org/10.1061/(ASCE)ST.1943-541X.0000954.
[11] Z. Zhang, J. Leng, X. Bian, T. Xie, T. Xu, A refined model for the flexural behavior of reinforced UHPC members under sustained loading, J. Build. Eng. 93 (2024) 109853, https://doi.org/10.1016/j.jobe.2024.109853.
[12] M.A. Modi, K.A. Patel, S. Chaudhary, Assessment of cracking, creep and shrinkage effects in indeterminate steel-concrete composite flexural members at service load, Structures 70 (2024) 107663, https://doi.org/10.1016/j.istruc.2024.107663.
[13] J. Davidovits, Geopolymer Chemistry and Applications, Geopolymer, Institute, 2008.
[14] A.A. Patil, H.S. Chore, P.A. Dode, Effect of curing condition on strength of geopolymer concrete, Adv. Concret. Construct. 2 (1) (2014) 29, https://doi.org/10.12989/acc.2014.2.1.029.
[15] J.S. Van Deventer, J.L. Provis, P. Duxson, Technical and commercial progress in the adoption of geopolymer cement, Miner. Eng. 29 (2012) 89–104, https://doi.org/10.1016/j.mineng.2011.09.009.
[16] S.E. Wallah, Creep behaviour of fly ash-based geopolymer concrete, Civil Eng. Dimens. 12 (2) (2010) 73–78, https://doi.org/10.9744/ced.12.2.73-78.
[17] A. Castel, S.J. Foster, T. Ng, J.G. Sanjayan, R.I. Gilbert, Creep and drying shrinkage of a blended slag and low calcium fly ash geopolymer concrete, Mater. Struct. 49 (2016) 1619–1628, https://doi.org/10.1617/s11527-015-0599-1.
[18] Z. Cheng, R. Zhao, Y. Yuan, F. Li, A. Castel, T. Xu, Ageing coefficient for early age tensile creep of blended slag and low calcium fly ash geopolymer concrete, Constr. Build. Mater. 262 (2020) 119855, https://doi.org/10.1016/j.conbuildmat.2020.119855.
[19] K. Sagoe-Crentsil, T. Brown, A. Taylor, Drying shrinkage and creep performance of geopolymer concrete, J. Sustain. Cement-Base. Mater. 2 (1) (2013) 35–42, https://doi.org/10.1080/21650373.2013.764963.
[20] J.L. Provis, J.S.J. Van Deventer (Eds.), Geopolymers: Structures, Processing, Properties and Industrial Applications, Elsevier, 2009, https://doi.org/10.1533/9781845696382.
[21] A. Castel, S. Foster, R. Gilbert, Serviceability of low creep fly ash geopolymer concrete beams, in: Proceedings of International Structural Engineering and Construction,, vol. 4, ISEC-9, Valencia, 2017, https://doi.org/10.14455/isec.res.2017.171, 1.
[22] Z.P. Bazant, R. L'Hermite, Mathematical modeling of creep and shrinkage of concrete. https://doi.org/10.1002/cnm.1630050609, 1988.
[23] J. Lubliner, J. Oliver, S. Oller, E. Onate, A plastic-damage model for concrete, Int. J. Solid Struct. 25 (3) (1989) 299–326, https://doi.org/10.1016/0020-7683(89)90050-4.
[24] F. Ding, Z. Yu, J. Ou, Constitutive model for uniaxial stress damage of concrete, J. Chang'an Univer. (Nat. Sci. Ed.) 28 (4) (2008) 70–73 (In Chinese).
[25] B. Singh, G. Ishwarya, M. Gupta, S.K. Bhattacharyya, Geopolymer concrete: a review of some recent developments, Constr. Build. Mater. 85 (2015) 78–90, https://doi.org/10.1016/j.conbuildmat.2015.03.036.
[26] A. Castel, R.I. Gilbert, Influence of time-dependent effects on the crack spacing in reinforced concrete beams, Struct. Concr. 15 (3) (2014) 373–379, https://doi.org/10.1002/suco.201300065.